

86/0112

APPLICATION OF GRID GENERATION TECHNIQUES TO
(i) COMPLEX GEOMETRIC SHAPES AND
(ii) HYPERSONIC LOW DENSITY FLOW FIELD IN
THE STAGNATION REGION OF A BLUNT BODY

by

MURALI. B,

TH
AE/1988/14
14931a

AE

1988

M

MUR

APP



DEPARTMENT OF AERONAUTICAL ENGINEERING

INDIAN INSTITUTE OF TECHNOLOGY, KANPUR

JANUARY, 1988

APPLICATION OF GRID GENERATION TECHNIQUES TO
(i) COMPLEX GEOMETRIC SHAPES AND
(ii) HYPERSONIC LOW DENSITY FLOW FIELD IN
THE STAGNATION REGION OF A BLUNT BODY

A Thesis Submitted
In Partial Fulfilment of the Requirements
for the Degree of

MASTER OF TECHNOLOGY

by

MURALI. B.

to the

DEPARTMENT OF AERONAUTICAL ENGINEERING

INDIAN INSTITUTE OF TECHNOLOGY, KANPUR

JANUARY, 1988

18 FEB 1988

CENTRAL LIBRARY

I. I. T., Kanpur.

Acc. No. **A 99702**

AE-1988-M-APP MUR-APP

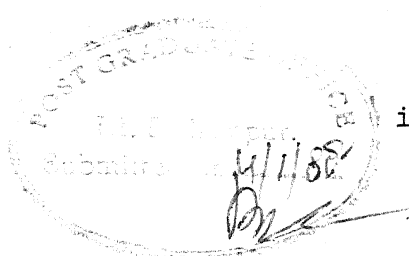
Thesis

620.0042

M93/a

To

AMMA, APPA, SEENU and KARTHI


iii)
4/1/88
D

CERTIFICATE

This is to certify that this work entitled
"APPLICATION OF GRID GENERATION TECHNIQUES TO (i) COMPLEX
GEOMETRIC SHAPES AND (ii) HYPERSONIC LOW DENSITY FLOW FIELD
IN THE STAGNATION REGION OF A BLUNT BODY" has been carried
out by Mr. MURALI.B, under my supervision and that this has
not been submitted elsewhere for obtaining a degree.

January, 1988.


(A.C. JAIN)
Professor

Department of Aeronautical Engineering
Indian Institute of Technology
Kanpur-208016, INDIA

ACKNOWLEDGEMENTS

I thank Dr. A.C. Jain, my thesis supervisor, for having taught me how to work productively. I thank him once again for the patience, affection and interest which he had exhibited during those memorable and stimulating discussions I had with him.

I thank Mr. G. Raghavan, one of my close friends for his invaluable help in the CAD Center.

I thank Mr. Ganguli, for the drawings and Mr. U.S. Mishra, for typing the manuscript.

-MURALI .B

CONTENTS

PAGE

ABSTRACT	v)
1. INTRODUCTION	1
2. GRID GENERATION USING ELLIPTIC PARTIAL DIFFERENTIAL EQUATIONS	6
1. Description	6
2. Mathematical Development	11
3. Control Functions	14
4. Numerical Implementation	17
5. Application of the Elliptic Grid Generation Techniques to Bodies of Complicated Shapes	19
(1) Elliptic Cylinder Containing a Circular Cylinder	19
(2) Aero-Assisted Orbital Transfer Vehicle	21
3. ADAPTIVE GRID GENERATION TECHNIQUE	32
(1) Description	32
(2) Mathematical Development	34
4. HYPERSONIC MERGED LAYER FLOW NEAR THE STAGNATION POINT OF A BLUNT BODY	37
1. Introduction	37
2. Mathematical Development	39
3. Numerical Method	54
4. Solution Procedure	58
5. Grid Adaptation	61
(1) Choice of the dependent Variable in the Weight Function	62
(2) Choice of the Constants A and B	63
6. Discussion of Results	65
TABLES	70
SUMMARY	73
REFERENCES	75

ABSTRACT

Grid generation technique using elliptic equations is discussed and applied to generate grids on complex geometries such as an elliptic cylinder containing a circular cylinder and an Aero-Assisted Flight Experiment Vehicle. The effect of the control functions on moving the grids to the desired locations is also discussed. It is hoped to couple this computer code with a flow field at some later stage.

Adaptive grid technique using equidistribution scheme is applied to the hypersonic stagnation point merged layer problem which had been analysed earlier on uniform grids by Jain and others. A weight function dependent upon a combination of the gradient and curvature of the profiles of temperature and normal component of velocity is used to place larger number of grids near the surface and in the outer shockwave like region. Computer code of Jain et al was accordingly modified and the resultant code was executed for shuttle flight conditions from an altitude of 104.93 Km to 85.74 Km. The results on adapted grids are compared with the results on uniform grids. It was found that upto a certain stagnation Reynolds number ($Re_O = \frac{\rho_\infty v_\infty r_B}{\mu(T_{O\infty})} = 160$) corresponding to shuttle flight conditions between 92 Km and 85 Km, the results with uniform grids and adapted grids are exactly the same. The computer took more time to execute the computer code

with adapted grids than with uniform grids. Within the range of stagnation Reynolds number $160 < Re \leq 260$ (corresponding to conditions between 92 Km and 85 Km), uniform grids gave converged but inaccurate results while adapted grids gave converged and physically plausible results. Beyond the value of stagnation Reynolds number of 260 and upto 430, computer code with uniform grids failed to converge while the computer code with adapted grids converged and gave physically plausible results. In this manner, adaptive grid technique extended the range of applicability of the merged layer approximation, from $Re = 160$ to almost three times its value. Also, computations with adapted and uniform grids were carried out on a cold wall and an insulated wall conditions with varied number of grid points. It was found that the number of grid points required with adapted grids to get the same accuracy is considerably less than that required with uniform grids. Consequently the computer time is considerably reduced.

APPLICATION OF GRID GENERATION TECHNIQUES TO

- (i) Complex Geometric Shapes and
- (ii) Hypersonic Low Density Flow Field in the Stagnation Region of a Blunt Body

CHAPTER 1INTRODUCTION

I. Grid generation techniques and grid adaptation techniques are the modern and powerful tools available to solve numerically a variety of problems involving complicated body shapes and large solution gradients in flow problems. One of the grid generation techniques which generates highly acceptable grids is the elliptic equations technique. Grid generation using elliptic equations tend to produce smooth grids but the grid lines may not be orthogonal every where and may be excessively skewed. Orthogonality near the surface can be imposed either by specifying the angle of the coordinate lines cutting the surface as proposed by Thompson⁴ or by using additional conditions as proposed by Coleman and Haussling⁶. Skewness can be controlled by the proper choice of the control functions in the Poisson equations. The advantages of grid generation techniques including elliptic differential equation technique are (i) the boundaries are represented by coordinate lines and (ii) the governing equations are solved in a rectangular computational domain irrespective of the shape of the physical domain. However, additional elliptic partial differential equations have to be solved in addition to

those governing the fluid flow.

Winslow¹ has initiated the elliptic grid generation technique which had been extensively studied by Thompson et al²⁻⁵.

In the present investigation, elliptic equations (both Laplace and Poisson) are used to generate grids about two problems (i) Elliptic cylinder enclosing a circular cylinder and (ii) Aero-Assisted Flight Experiment Vehicle. For the time being, grids generated here have not been coupled with any flow problem.

II. Due to inadequate resolution of gradients, inaccurate solutions are obtained when a flow problem solved on a uniform grid, has large solution gradients whose location is not known a priori. These gradients can be resolved more satisfactorily by making the grids dependent on the solution gradients (or/and curvatures) and allowing the grid in the physical domain to evolve along with the solution. This is called adapting the grid. The grids in the computational domain is rectangular, and uniform. The governing equations are solved on the uniform grids in the computational domain.

Brackbill and Saltzman⁸ had shown from variational principles that the solution error will be a minimum if the quantity wJ^2 is equal to the same constant throughout the mesh, where w is a weight function which is dependent

on the solution gradients (or/and curvatures) and J is the Jacobian of the transformation between the physical and computational domains. This leads to the equidistribution scheme in the one dimensional case where the minimisation of the integral corresponding to the quantity wJ^2 is analogous to minimising the energy of a system of tension springs, connected in series with each other with spring constants w .

White⁸, Dwyer et al^{9,10}, Rai and Anderson¹¹, Gnoffo¹², Nakahashi and Deiwert^{13,14} and Abolhassani et al¹⁵ have developed the equidistribution idea with different weight functions and applied to specific problems to show the robustness of the method in resolving sharp solution gradients. Nakahashi and Deiwert^{13,14} have also developed a procedure for two¹⁴ and three¹³ dimensional adaptation using torsion spring analogy in addition to tension spring analogy. Abolhassani et al¹⁵ have given a form of the weight function which is dependent on more than one solution variable.

In hypersonic low density flow, the present approach catches the shock wave like structure as part of the computational domain. Thus large gradients of the flow variables occur near the surface and also in the outer region where a shock wave like structure is formed. The location of the shock wave in the flow field is not known a priori. Hence adaptive grid generation technique

seems to be the appropriate technique for solving the merged layer problem.

The following form of the weight function, as proposed by Dwyer⁸, is used in this investigation:

$$w(\xi) = 1 + A \left| \frac{df}{d\xi} \right| + B \left| \frac{d^2f}{d\xi^2} \right|$$

where ξ is the computational coordinate line in the computational domain and f is the dependent variable which is chosen as the temperature near the surface and the normal component of velocity away from the surface.

Numerical experimentation with various dependent variables indicated the above combination along with $A = 1$ and $0.05 \leq B \leq 0.4$, give the best resolution of the flow field.

Following Nakahashi and Deiwert¹⁴, the grid interval in the physical plane is related to the weight function in the computational plane by the following relation,

$$\Delta x_i = \frac{L}{w(\xi_i) \sum_{i=1}^N \frac{1}{w(\xi_i)}}$$

where $L = \sum_{i=1}^N \Delta x_i$, N being the total number of grid points.

Merged layer problem has been extensively analysed and studied on a uniform grid by Jain¹⁶⁻¹⁹, Jain and Adimurthy²⁰⁻²², Kumar and Jain^{23,24}, Jain and Kumar²⁵, Jain and Saroj Prabha^{26,27}, Jain and Woods²⁸ and Singh and Jain²⁹. In all the above investigations, and in the current work flow in the merged layer is described by using the full Navier-Stokes equations. Levinski and Yoshihara³⁰ had earlier solved the same problem using thin shock layer approximation of the NS equation.

With adaptation, it is found that (i) the range of applicability of the merged layer theory can be extended to a much denser region of the atmosphere (ii) the accuracy of the solution has increased in the range of prescribed parameters where uniform grids do not give satisfactory results. (iii) Solution with adapted grids can be obtained with the same accuracy as the solution with uniform grids using lesser number of grid points, thereby reducing computer memory and time.

CHAPTER 2

GRID GENERATION USING ELLIPTIC PARTIAL DIFFERENTIAL EQUATIONS

2.1 Description

The first step in solving boundary value problem numerically, is to generate suitable grids in the physical domain so that the boundary is properly represented. Prior to the introduction of boundary fitted coordinate system, only Cartesian coordinates were used to solve problems involving arbitrary bodies where the boundary is placed between grid points and values of the dependent variables and the boundary conditions are interpolated onto the boundary. In most boundary value problems this interpolation has led to large errors in the solution of the governing equations. Such large errors especially occur in the cases of bodies involving large curvatures or/and slope discontinuities. The avoidance of interpolation is the major advantage of using boundary conforming coordinates.

Transformation relations have to be obtained in order to represent the physical domain using boundary conforming coordinates (ξ, η) which is already represented by the Cartesian coordinates (x, y) . In general, lines of constant- ξ and constant- η , in the physical domain, are non-orthogonal curvilinear coordinate lines. But in the computational domain the same lines of constant- ξ and constant- η are straight lines and the physical domain in

the transformed plane (or in the computational plane) becomes a rectangle. The intersections of the lines of constant- ξ and constnt- η give the grid point locations. In the computational plane the grid intervals, $\Delta\xi$ and $\Delta\eta$, are always taken as unity in both the directions , ξ and η . The actual values of the curvilinear coordinates ξ and η are immaterial to the subsequent use of this coordinate system in the numerical solution of partial differential equations, for the grid intervals, $\Delta\xi$ and $\Delta\eta$, simply cancel out of all difference expressions for the transformed derivatives. The governing equations are always solved in the computational plane and the solution in the physical plane is obtained by incorporating the metric terms of the transformations in the governing equations.

Some of the restrictions which must be imposed on the transformation relations are (i) there should be one-to-one correspondence between the physical and computational planes, (ii) lines on which one of the coordinate is constant, the other must vary monotonically (iii) lines of constant- ξ (or constant- η) should not cut each other(iv) coordinate lines must be smooth and (v) there should not be any void in the physical plane.

Thus the problem of grid generation boils down to finding the transformations between the physical and computational domains. The various methods of grid

generation differ only by the manner by which these transformations are defined. In the case of algebraic grid generation the transformation relationship between the physical and computational plane is mentioned explicitly, either analytically or numerically. The initial grids which are used in this investigation to generate the solutions of the elliptic equations are examples of algebraic grid generation technique where the relationship is fixed numerically.

Consider Fig. (2.1), Fig. (2.1a) shows the physical plane where two arbitrary curves Γ_1 and Γ_2 represent the inner and outer boundaries. It is required to generate a boundary fitted coordinate system in the domain between them. For this a cut is made arbitrarily in between them at $\theta = 0$ (chosen arbitrarily). The inner body is assigned a value of η , say $\eta = 1$. The outer body is assigned another value of η , say $\eta = J$. One edge of the cut, represented by Γ_3 is assigned a value of ξ , say $\xi = 1$ and the other edge of the cut, represented by Γ_4 is assigned another value of ξ , say $\xi = I$. All the remaining values of η , from $\eta = 2$ to $\eta = J-1$ and ξ , from $\xi = 2$ to $\xi = I-1$ are assigned arbitrarily along the various curves in the physical domain confined between Γ_1 and Γ_2 as shown in Fig. 2.1. Thus the physical domain after this transformation becomes the rectangular domain in the computational plane.

Conceptually the physical domain can be considered to have opened at the cut $\theta = 0$ and then deformed into a rectangular domain. This implies that the boundaries on which $\xi = 1$ and $\xi = J$ in the computational plane becomes reentrant on each other in the physical plane and therefore the boundary conditions need not be and should not be specified on them.

So, it could be seen that boundary conditions are specified on all boundaries where it could be specified (i.e. on lines with $\eta = 1$ and $\eta = J$). Such a problem could obviously be solved using an elliptic system of partial differential equations.

From variational principles, smooth grid lines are given by the minimisation of the following integral

$$I_s = \int [(\nabla \xi)^2 + (\nabla \eta)^2] dx dy \quad (2.1)$$

in two-dimensions. Consider

$$I_1 = \int_D (\nabla \xi)^2 dx dy \quad (2.2)$$

In two-dimensions,

$$\nabla \xi = i \frac{\partial \xi}{\partial x} + j \frac{\partial \xi}{\partial y}$$

which yields

$$(\nabla \xi)^2 = \left(\frac{\partial \xi}{\partial x}\right)^2 + \left(\frac{\partial \xi}{\partial y}\right)^2$$

Hence, equation (2.2) becomes

$$I_1 = \iint_D \left\{ \left(\frac{\partial \xi}{\partial x}\right)^2 + \left(\frac{\partial \xi}{\partial y}\right)^2 \right\} dx dy \quad (2.3)$$

In general, if

$$I = \iint_D F(x, y, z, \frac{\partial z}{\partial x}, \frac{\partial z}{\partial y}) dx dy$$

then minimisation of I leads to the Euler-Lagrange is equation

$$F_z - \frac{\partial}{\partial x} \{F_p\} - \frac{\partial}{\partial y} \{F_q\} = 0 \quad (2.4)$$

where

$$p = \frac{\partial z}{\partial x}, \quad q = \frac{\partial z}{\partial y}$$

$$\frac{\partial}{\partial x} \{F_p\} = F_{px} + F_{pz} \frac{\partial z}{\partial x} + F_{pp} \frac{\partial p}{\partial x} + F_{pq} \frac{\partial q}{\partial x} \quad (2.5)$$

and

$$\frac{\partial}{\partial y} \{F_q\} = F_{qy} + F_{qz} + \frac{\partial z}{\partial y} + F_{qp} \frac{\partial p}{\partial y} + F_{qq} \frac{\partial q}{\partial y} \quad (2.6)$$

In equations (2.4), (2.5) and (2.6) suffixes denote differentiation.

Applying the Euler-Lagrange equation (2.4) to minimise the integral I_1 in equation (2.3), one gets

$$\nabla^2 \xi = 0 \quad (2.7)$$

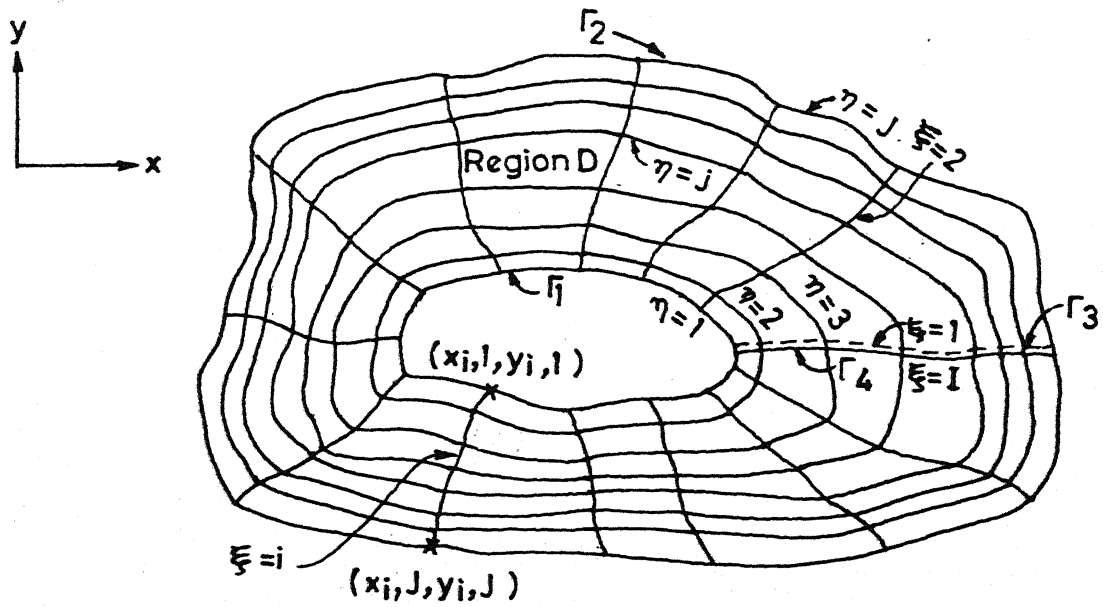
By adopting a similar procedure for the other coordinate line η , one gets

$$\nabla^2 \eta = 0 \quad (2.8)$$

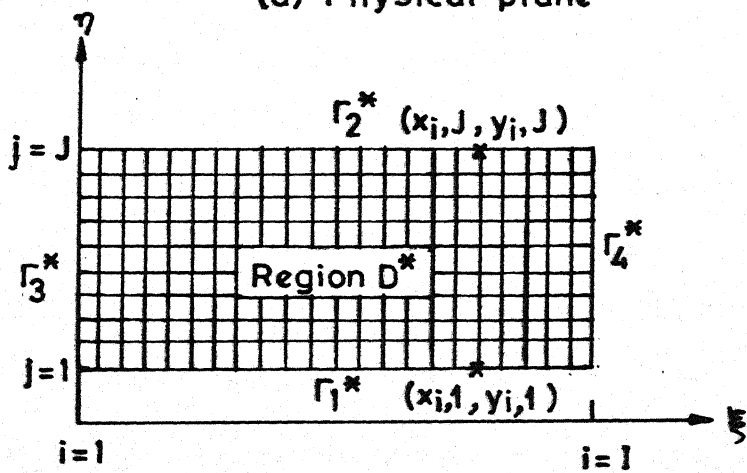
Thus, minimisation of the integral (2.1) yields, equations (2.7) and (2.8), which are the familiar Laplace equations and they are elliptic in nature. It was mentioned earlier that the given problem of grid generation in the physical plane can be solved by using a system of elliptic equations and now it is shown that the particular form of the elliptic equations, to obtain smooth grid lines, is the Laplace equations or more generally it could be the Poisson equations.

2.2 Mathematical Development

Transforming the two-dimensional, doubly connected region D , (physical plane) bounded by two simple, closed arbitrary contours, Γ_1 (inner boundary) and Γ_2 (outer boundary), onto a rectangular region D^* (computational plane) as illustrated in Fig. (2.1). is considered here.



(a) Physical plane



(b) Transformed plane

FIG. 2.1 FIELD TRANSFORMATION - SINGLE BODY

It is required that Γ_1 map onto Γ_1^* , Γ_2 onto Γ_2^* , Γ_3 onto Γ_3^* and Γ_4 onto Γ_4^* . It is to be noted that Γ_1^* and Γ_2^* are required to be constant η -lines, while the arbitrary cut between contours Γ_1 and Γ_2 (i.e. Γ_3 and Γ_4) becomes oconstant ξ -lines.

If it is required to generate the curvilinear coordinates (ξ, η) in the physical plane, then, the elliptic system is of the form

$$\xi_{xx} + \xi_{yy} = p(\xi, \eta) \quad (2.9)$$

$$\eta_{xx} + \eta_{yy} = Q(\xi, \eta)$$

with Dirichlet boundary conditions, one coordinate being specified to be equal to a constant on the inner boundary and equal to another constant on the outer boundary, with the other coordinate varying monotonically over the same range around both the inner boundary and the outer boundary. Note that in the above equations ξ and η are the dependent variables.

Since the grids in the physical domain is unknown and it is desired to perform all numerical computations in the uniform rectangular transformed plane, the dependent and independent variables must be interchanged in equation (2.9). This results in the coupled system

$$\alpha x_{\xi\xi} - 2\beta x_{\xi\eta} + \gamma x_{\eta\eta} = -J^2 [x_{\xi} p(\xi, \eta) + x_{\eta} q(\xi, \eta)] \quad (2.10)$$

$$\alpha y_{\xi\xi} - 2\beta y_{\xi\eta} + \gamma y_{\eta\eta} = -J^2 [y_{\xi} p(\xi, \eta) + y_{\eta} q(\xi, \eta)]$$

where

$$\alpha = x_{\eta}^2 + y_{\eta}^2, \quad \gamma = x_{\xi}^2 + y_{\xi}^2$$

$$\beta = x_{\xi} x_{\eta} + y_{\xi} y_{\eta}, \quad J = x_{\xi} y_{\eta} - x_{\eta} y_{\xi}$$

with the transformed boundary conditions

$$\begin{pmatrix} x \\ y \end{pmatrix} = \begin{pmatrix} f_1(\xi, 1) \\ f_2(\xi, 1) \end{pmatrix}, [\xi, 1] \in \Gamma_1^* \quad (2.11)$$

$$\begin{pmatrix} x \\ y \end{pmatrix} = \begin{pmatrix} g_1(\xi, J) \\ g_2(\xi, J) \end{pmatrix}, [\xi, J] \in \Gamma_2^*$$

The functions f_1 , f_2 , g_1 and g_2 are specified by the known shape of the contours Γ_1 and Γ_2 and the specified distribution of ξ thereon. As noted, boundary data are neither required nor allowed along the reentrant boundaries Γ_3^* and Γ_4^* . In equation (2.11) J denotes the number of grid points in the η -direction.

The system given by the equations (2.10) is a quasi-linear elliptic system for the physical coordinate functions, $x(\xi, \eta)$ and $y(\xi, \eta)$, in the transformed plane. Although this system is considerably more complex than that given by equation (2.9), the boundary conditions are specified on straight boundaries and the coordinate spacing in the transformed plane is uniform. The boundary-fitted coordinate system generated by the solution to (2.10) has a constant η -line coincident with each boundary in the physical plane. The $\xi =$ constant lines may be spaced as desired around the boundaries, since the assignment of the ξ -values to the $[x, y]$ boundary points via the functions f_1 , f_2 , g_1 and g_2 is arbitrary. (Numerically, the discrete boundary values $[x_k, y_k]$ are transformed to equispaced discrete ξ_k - points on both boundaries). Control of the spacing of the $\eta =$ constant lines and of the incidence angle of the $\xi =$ constant lines at the boundaries is accomplished by varying the functions $p(\xi, \eta)$ and $Q(\xi, \eta)$ in (2.10).

2.3 Control Functions

The functions P and Q are called control functions as they control the positioning of the curvilinear coordinate lines. When both P and Q are zero, the resulting equations are the well known Laplace equations. With the Laplace equations the coordinate lines in the physical plane will tend to be equally spaced in the absence

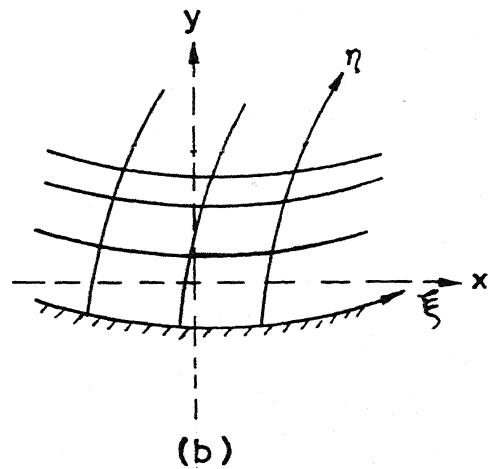
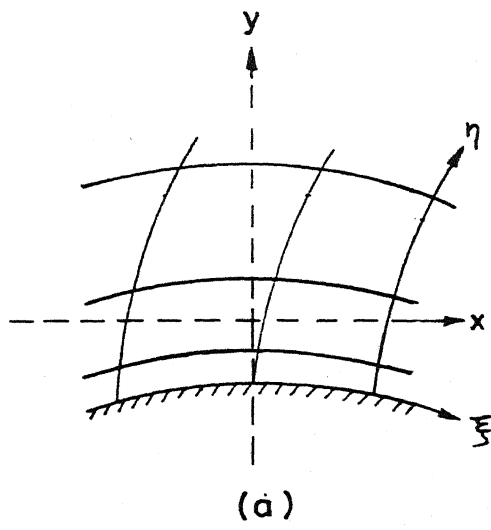


FIG. 2.2

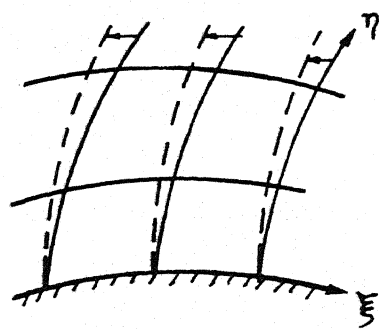
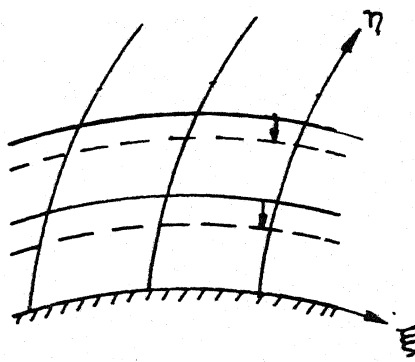


FIG. 2.3

FIG. 2.2 COORDINATE LINES NEAR A (a) CONVEX BOUNDARY
AND (b) CONCAVE BOUNDARY

FIG. 2.3 EFFECT OF P AND Q IN MOVING THE COORDINATE
LINES

boundary curvature because of the strong smoothing effect of the Laplacian. They will be more closely spaced over convex boundaries and less so over concave boundaries as illustrated in Fig. 2.2. On the convex surface, Fig. 2.2a, it could be seen that $\eta_{xx} > 0$, because of the convex curvature of the lines of constant η . Therefore it follows that $\eta_{yy} < 0$, and hence the spacing between the η -lines must increase with y . The η -lines will tend to be more closely spaced over such a convex boundary segment. For concave segments, illustrated in Fig. (2.2b), it could be seen, $\eta_{xx} < 0$, so that $\eta_{yy} > 0$, and hence the spacing of the η -lines must decrease outward from this concave boundary.

Now, suppose that both P and Q are non-zero. In such cases, negative values of the function Q will cause the η -lines to tend to move in the direction of decreasing η while negative values of P will cause ξ -lines to tend to move in the direction of decreasing ξ . These effects are illustrated in Fig. (2.3) for an η -line boundary. One particularly effective procedure is to choose P and Q as exponential terms and this procedure is followed in this work. The coordinates are generated as the solution of equation (2.10) with $P(\xi, \eta)$ and $Q(\xi, \eta)$ given by the following expressions :

$$\begin{aligned}
 P(\xi, \eta) &= - \sum_{i=1}^n a_i \operatorname{sign}(\xi - \xi_i) \exp(-c_i |\xi - \xi_i|) \\
 &\quad - \sum_{j=1}^m b_j \operatorname{sign}(\xi - \xi_j) \exp(-d_j ((\xi - \xi_j)^2 + (\eta - \eta_j)^2)^{1/2}) \\
 Q(\xi, \eta) &= - \sum_{i=1}^n a_i \operatorname{sign}(\eta - \eta_i) \exp(-c_i |\eta - \eta_i|) \\
 &\quad - \sum_{j=1}^m b_j \operatorname{sign}(\eta - \eta_j) \exp(-d_j ((\xi - \xi_j)^2 + (\eta - \eta_j)^2)^{1/2}),
 \end{aligned}
 \tag{2.12a}$$

(2.12b)

where the positive amplitudes and decay factors are not necessarily the same in the two equations. Here the first terms have the effect of attracting the $\xi = \text{constant}$ lines to the $\xi = \xi_i$ lines in equation (2.12a), and attracting $\eta = \text{constant}$ lines to the $\eta = \eta_i$ lines in equation (2.12b). The second terms cause $\xi = \text{constant}$ lines to be attracted to the point (ξ_i, η_i) in (2.12a) with similar effect on $\eta = \text{constant}$ lines in (2.12b).

Moreover, the grids can be made to depend on the solution of the governing equations by incorporating the solution variables in the functions P and Q. It is interesting to note that this becomes some sort of adaptive grid technique, in such cases.

2.4 Numerical Implementation

All the derivatives in equation (2.10) are approximated by second order central difference expressions

$$(f_\xi)_{ij} \cong \frac{1}{2} (f_{k1,j} - f_{k2,j})$$

$$(f_\eta)_{ij} \cong \frac{1}{2} (f_{i,j+1} - f_{i,j-1})$$

$$(f_{\xi\xi})_{ij} \cong f_{k1,j} - 2f_{i,j} + f_{k2,j}$$

$$(f_{\eta\eta})_{ij} \cong f_{i,j+1} - 2f_{i,j} + f_{i,j-1}$$

$$(f_{\xi\eta})_{ij} \cong \frac{1}{4} (f_{k1,j+1} - f_{k1,j-1} - f_{k2,j+1} + f_{k2,j-1})$$

k_1 and k_2 are described below.

The resulting set of $2I(J-1)$ non-linear difference equations, two for each point (i,j) for $i = 1, 2, 3, \dots, I$ and $j = 2, 3, 4, \dots, J-1$, are solved by successive accelerated replacement (SAR) method which is described in the numerical implementation section of the merged layer problem to follow. To solve the equations by SAR method an initial grid has to be developed in the physical plane. The generation of the initial grid is described in the section on application of the differential equation method.

It is to be noted that both the lines corresponding to $i = 1$ and $i = I$ represent the cut in the physical domain. In other words the same line which represents the cut in the physical domain is represented by two lines corresponding to

$i = 1$ and $i = I$ in the computational domain. So when calculating the derivatives corresponding to $i = 1$ and $i = I$, k_1 is taken to be 2 and k_2 is taken be $I-1$. For all other values of i , $k_1 = i+1$ and $k_2 = i-1$.

Convergence:

SAR method is applied to one ξ -line at a time from $i = 1$ to $i = I$. Both the values of x and y are changed along a line. When the maximum error among the values of x and y along the line is less than the prescribed limit of 10^{-4} , then the solution is considered to have converged along that line and the next line is taken. In this way convergence is attained on all the ξ -lines from $i = 1$ to $i = I$. Now since lines corresponding to $i = 1$ and $i = I$ represent the same physical line, the maximum error in the values of the difference of x and y for these two lines is found. If the error is less than the prescribed limit of 10^{-4} than the solution is considered to have converged globally. Otherwise the whole cycle is again started with $i = 1$, until global convergence is attained. If the solutions do not converge to the prescribed limit in 15 cycles for the elliptical cylinder containing a circular cylinder problem and 60 cycles for the AFE vehicle problem, but the error decreases continuously, then the solution at the end of 15 and 60 cycles are accepted as reasonable for the respective cases.

2.5 Application of the Elliptic Grid Generation Technique to Bodies of Complicated Shapes

(1) Elliptical Cylinder containing a Circular Cylinder:

This problem in two-dimensions becomes an ellipse containing a circle. It is desired to generate grids in the domain bounded by an ellipse, $\frac{x^2}{r_1^2} + \frac{y^2}{r_2^2} = 1$, with $r_1 = 6$ units and $r_2 = 4$ units and a circle $(x-a)^2 + (y-b)^2 = r^2$, with $r = 2$ units and (a,b) varied among $(0,0)$, (1.0) , $(0, 0.5)$ and $(1, 0.5)$, Figs (2.4)-(2.9), by solving equations (2.10) with both P and Q as zero and with the following boundary conditions:

(i) On the inner boundary, $\eta = 1$,

$$x_{i,1} = r(\eta=1) \cos [\theta(\xi_i)] \quad , \quad i = 1, 2, 3, \dots, I$$

$$y_{i,1} = r(\eta=1) \sin [\theta(\xi_i)]$$

(ii) On the outer boundary, $\eta = J$

$$x_{i,J} = r_1(\eta=J) \cos [\theta(\xi_i)] \quad , \quad i = 1, 2, 3, \dots, I$$

$$y_{i,J} = r_2(\eta=J) \sin [\theta(\xi_i)]$$

where the functions $r(\eta)$, $r_1(\eta)$, $r_2(\eta)$ and $\theta(\xi)$ on the boundaries $\eta = 1$ and $\eta = J$ are specified numerically.

For example, the boundary values of x and y at $(i, 1)$ in the computational plane are $(x_{i,1})$ and $y_{i,1}$ respectively for all values of i . Similarly, at the point (i, J) they are $x_{i,J}$ and $y_{i,J}$ respectively for all values of i . The physical plane thus gets transformed to a rectangle in the computational plane.

Initial Grid:

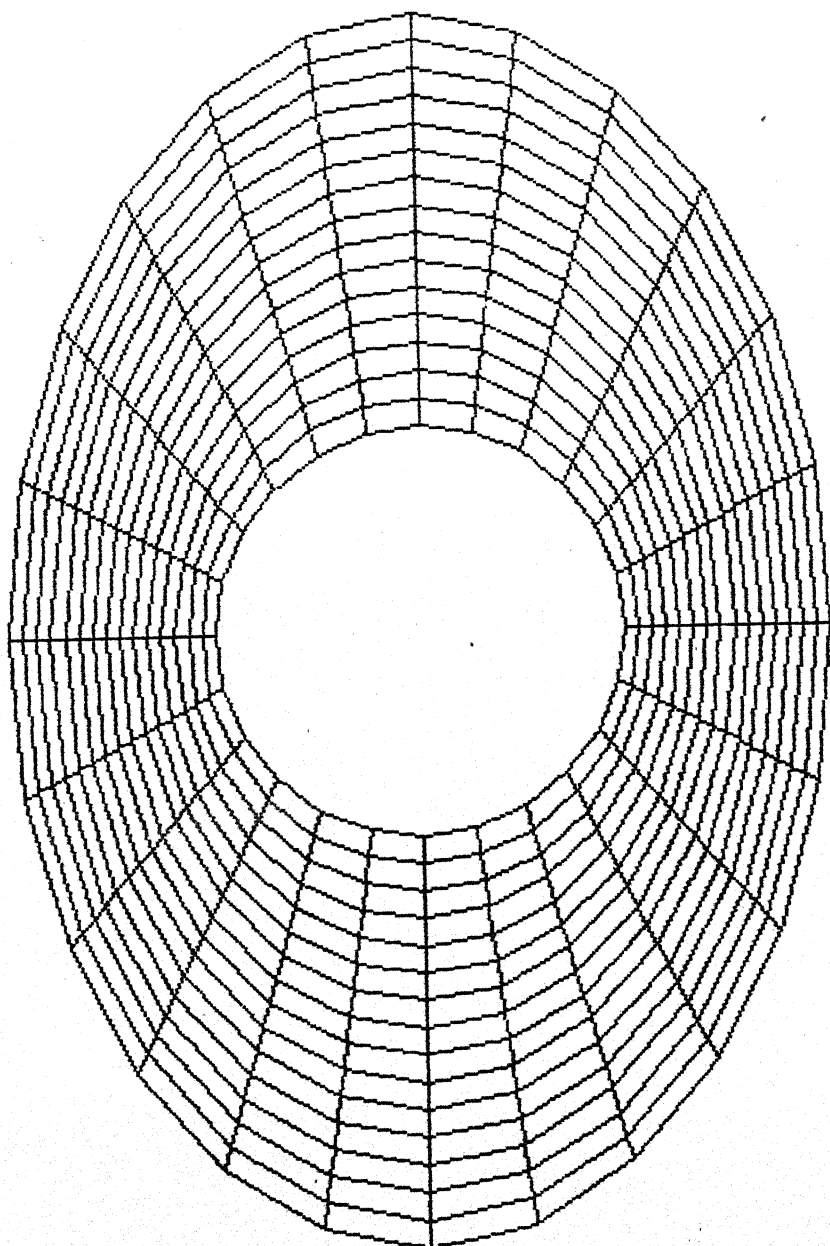
With $\Delta\theta = 15^\circ$, 25 grid points are chosen on the inner boundary, starting from $\theta = 0^\circ$ and ending at $\theta = 360^\circ$, using equations (2.13a). Similarly 25 points are chosen on the outer boundary. θ is increased in the anti-clockwise direction. Each point $(x_{i,1}, y_{i,1})$ on the inner boundary is connected to the corresponding point $(x_{i,J}, y_{i,J})$ on the outer boundary by a straight line. These lines represent constant- ξ lines. Each constant- ξ line is divided into $(J-1)$ equal parts (with $J = 16$) so that there will be J number of grid points on each line. The (x, y) coordinate of the j^{th} grid point on the i^{th} grid line is given by

$$x_{i,j} = \frac{(j-1)x_{i,J} + (J-j)x_{i,1}}{(J-1)}, \quad j = 2, 3, 4, \dots, (J-1) \quad (2.14a)$$

$$y_{i,j} = \frac{(j-1)y_{i,J} + (J-j)y_{i,1}}{(J-1)}, \quad j = 2, 3, 4, \dots, (J-1) \quad (2.14b)$$

Now by keeping $j = \text{constant}$ and varying i , all the points $(x_{i,j}, y_{i,j})$ are joined with each other. For each value of j from $j = 2$ to $j = J-1$, this is repeated. These lines are the constant- η lines.

FIGURE 2.4 Centre of the Circle at the Origin-Initial Grid



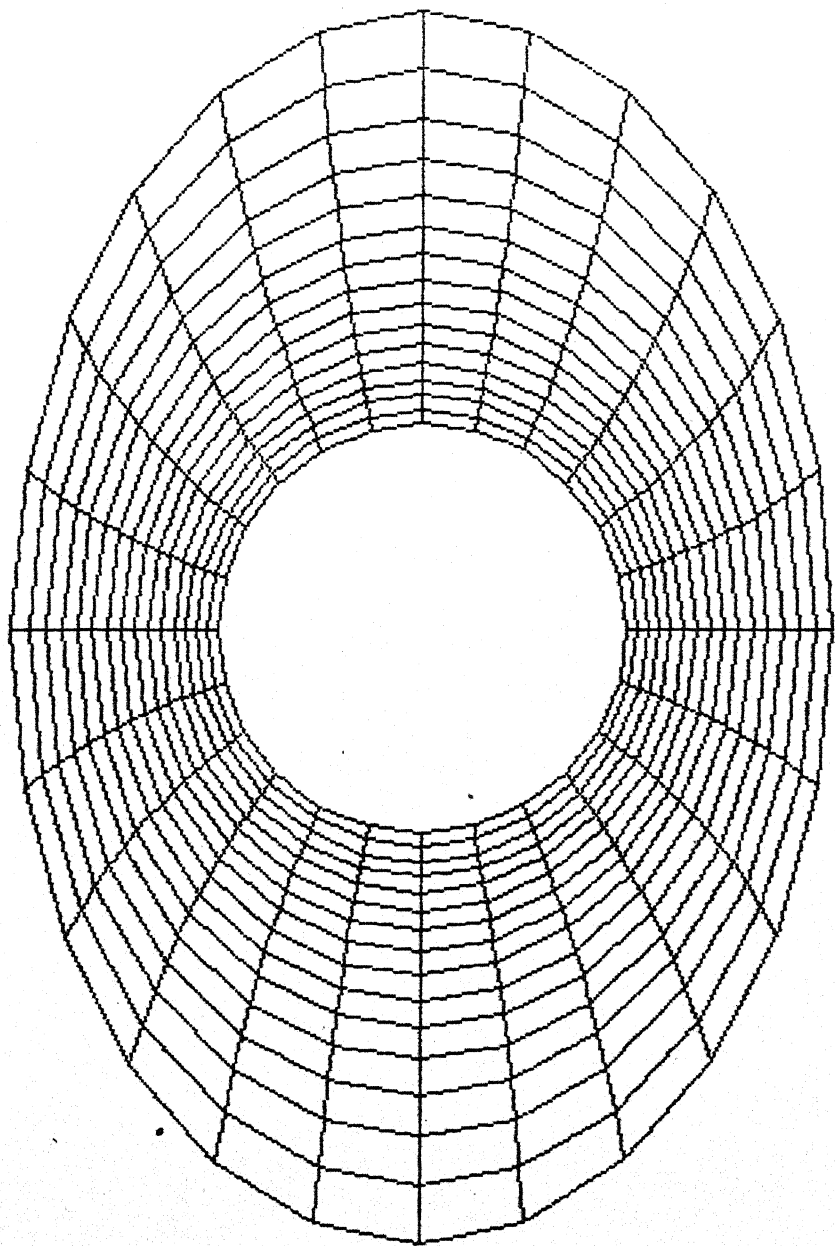


FIGURE 2.5 Centre of the Circle at the Origin-Laplace Solution

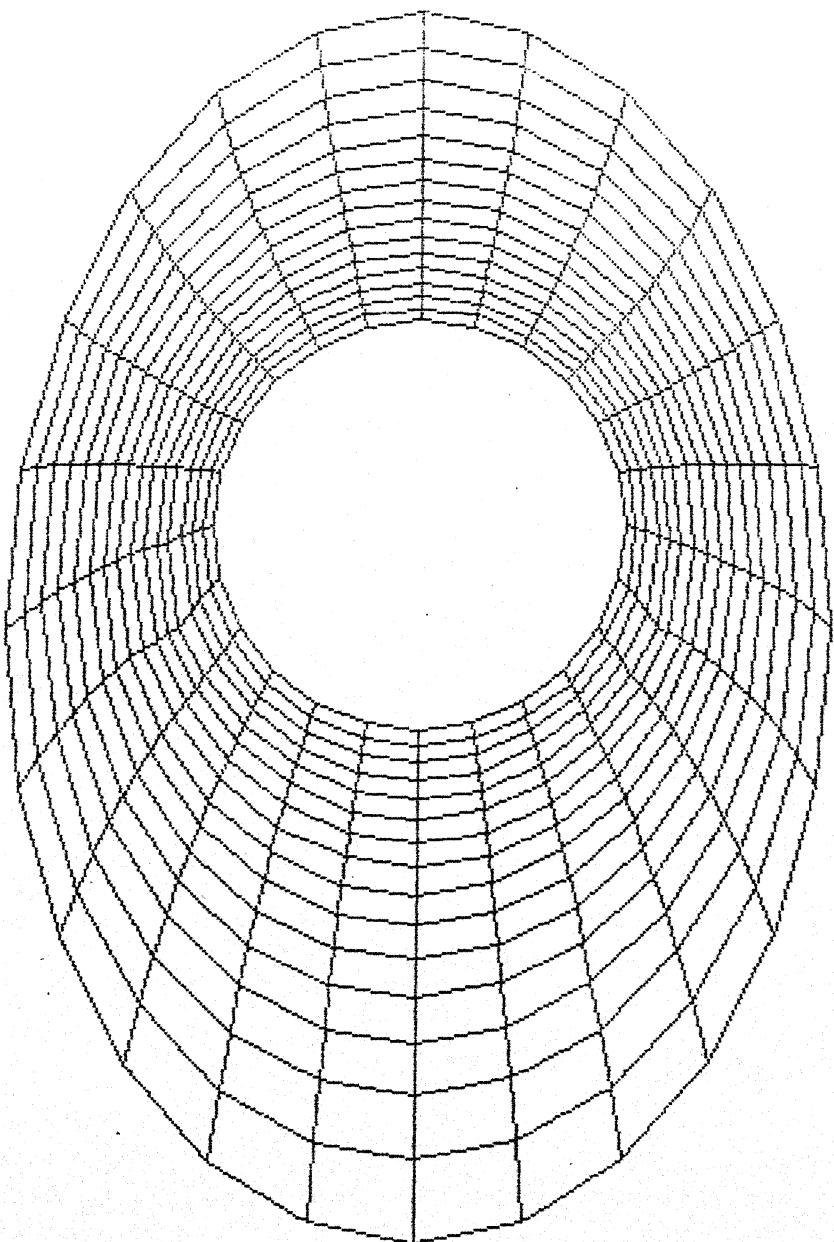


FIGURE 2.6 Centre of the Circle at $(1,0)$ -Laplace Solution

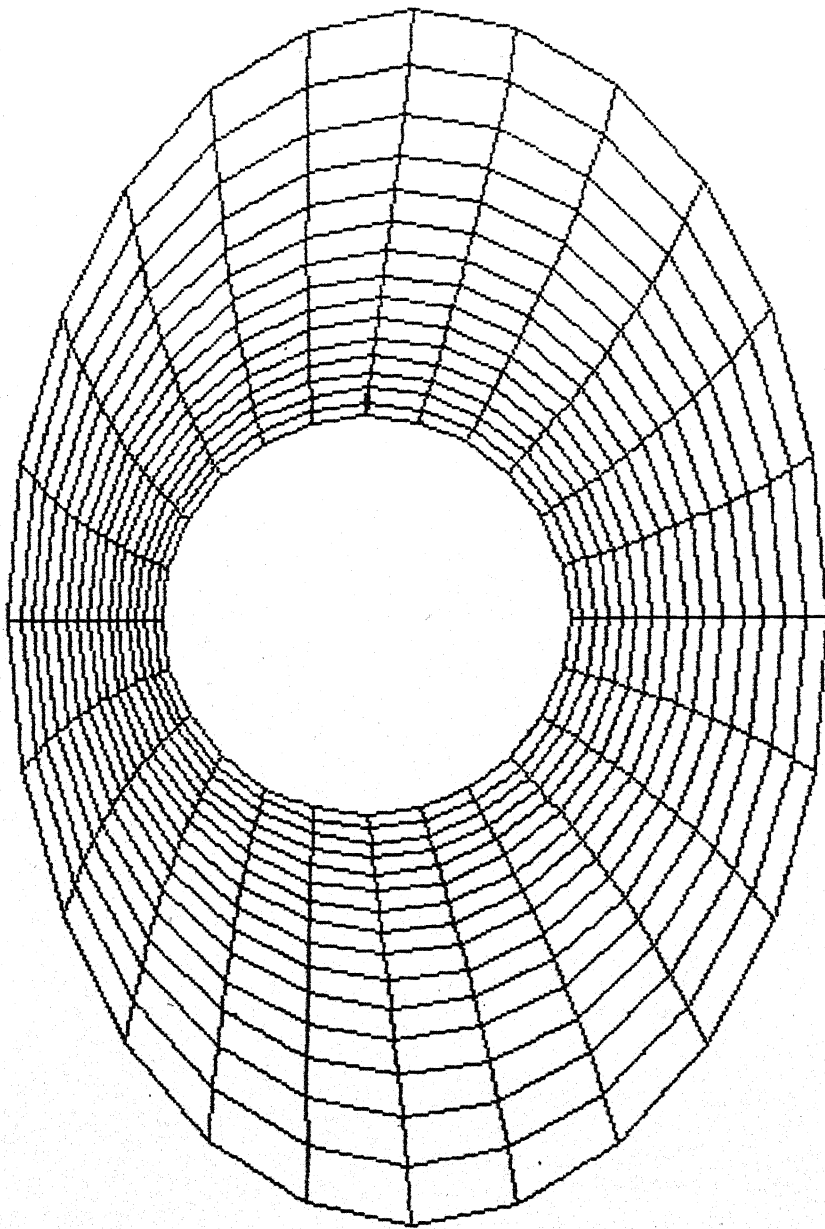


FIGURE 2.7 Centre of the Circle at $(0, 0, 5)$ -Laplace Solution

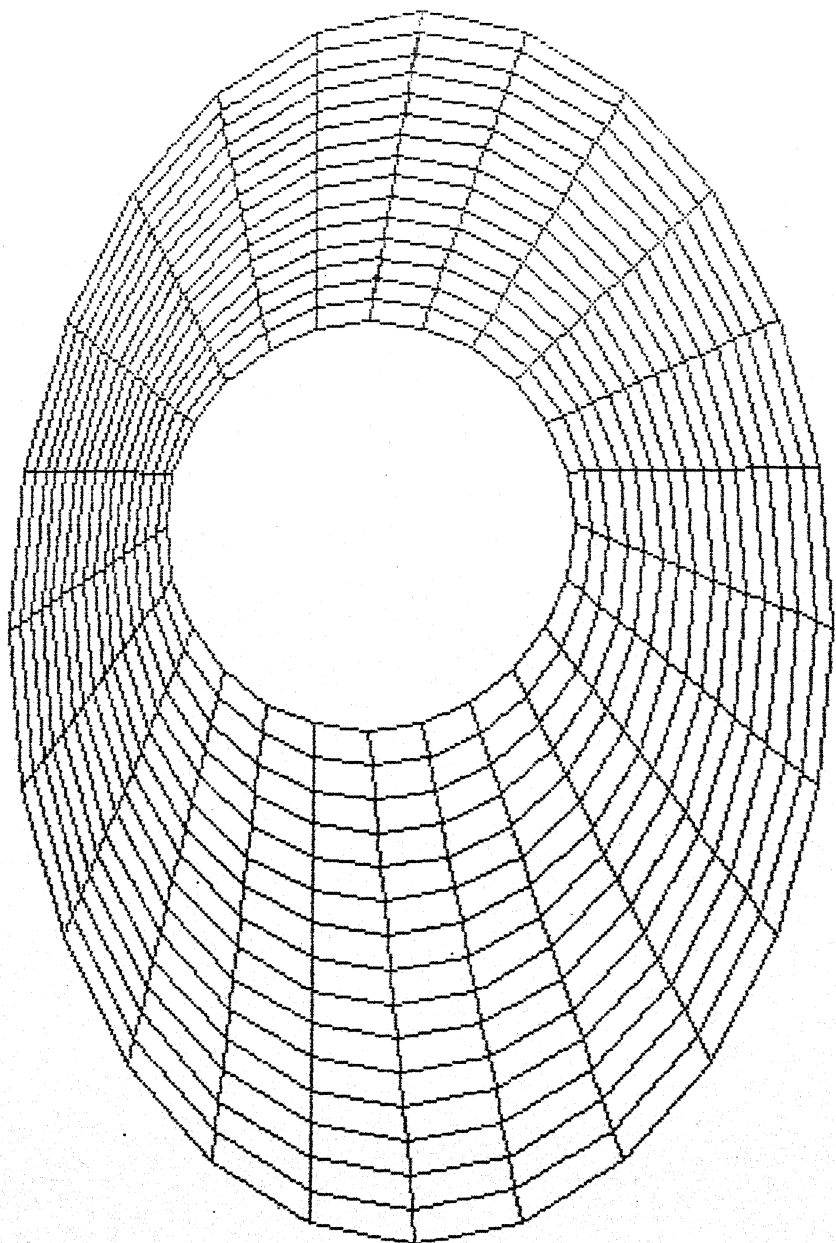


FIGURE 2.8 Centre of the Circle at $(1, 0.5)$ -Initial Grid

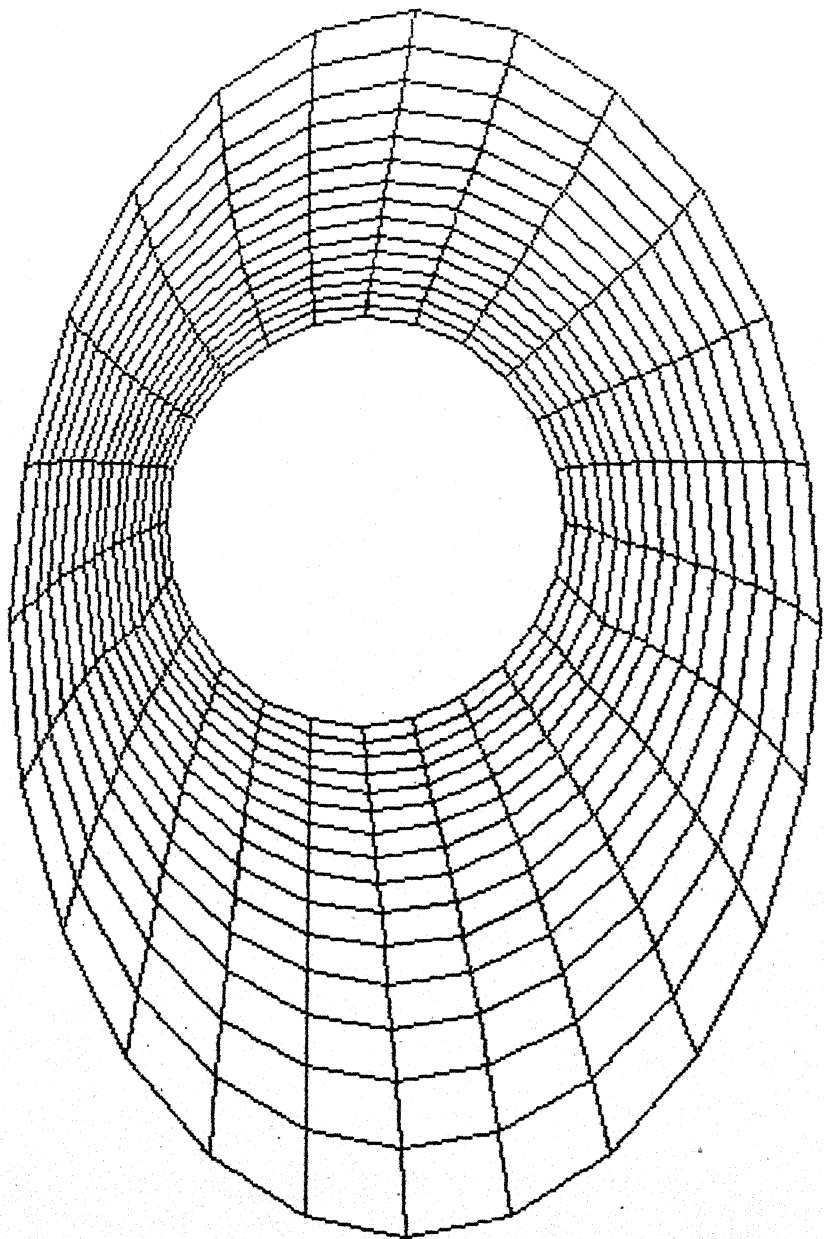


FIGURE 2.9 Centre of the Circle at $(1, 0.5)$ -Laplace Solution

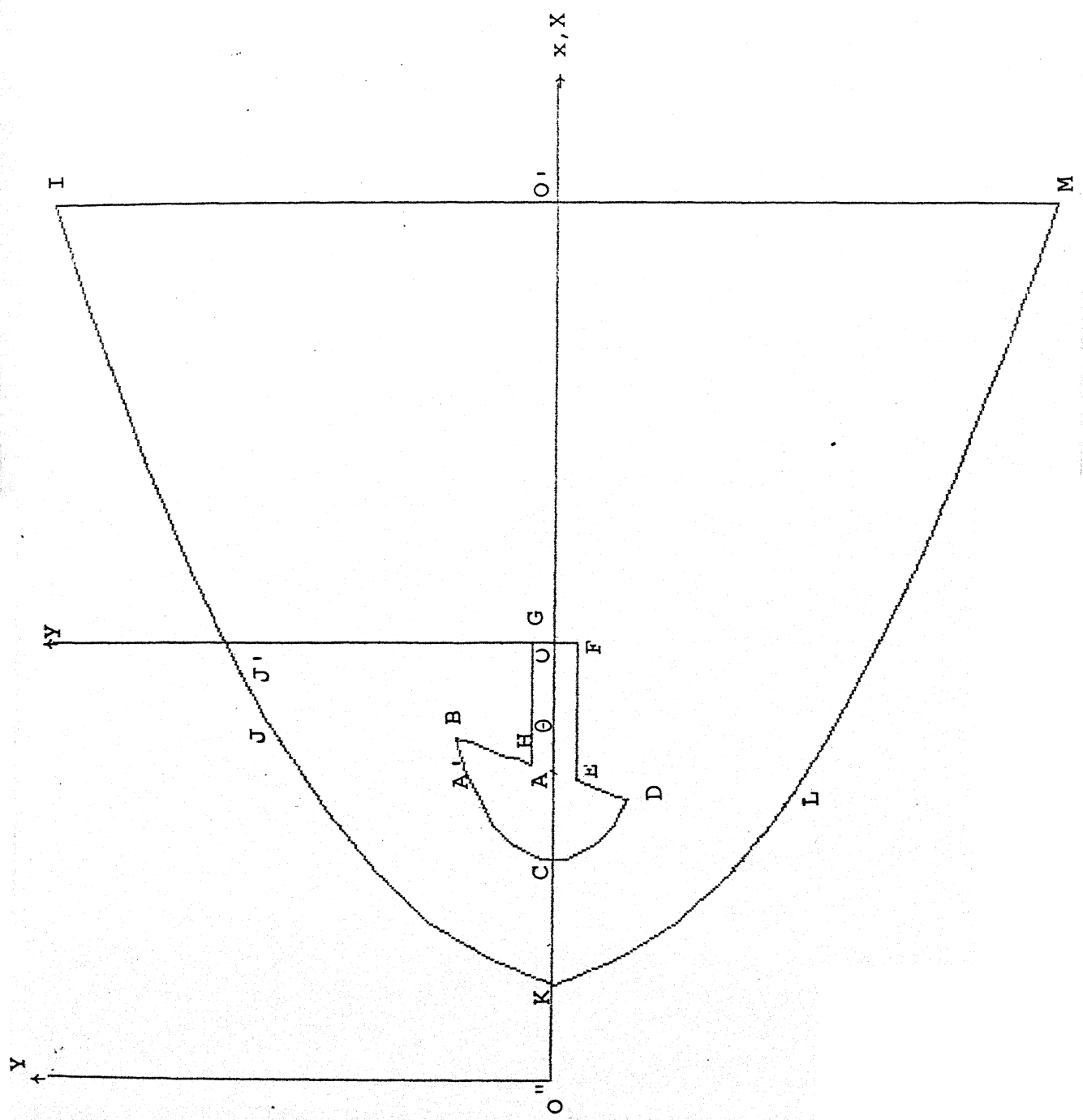


FIGURE 2.10 Aero-Assisted Flight Experiment Vehicle

Results:

Initial grids are shown in Fig.(2.4) and Fig. (2.8) for the cases when the centre of the circle, (a,b) lies at (0.0) and (1, 0.5). Final grids are shown in Figs.(2.5), (2.6), (2.7) and (2.9), when the centre (a,b) lies at (0.0), (1.0), (0,0.5) and (1,0.5) respectively. By comparing the final grids with the initial grids it could be seen that the η -lines near the inner boundary are almost circular in shape and those near the outer boundary are nearly elliptical in shape. This is due to the inherent smoothing nature of the Laplace equations. CPU-time taken in the ND-500 system of the CAD-center is about a minute.

(2) Aero-Assisted Flight Experiment Vehicle:

In order to investigate the flow characteristics around a reentering vehicle, NASA is planning to carry out exhaustive flight experiments using a vehicle similar to the one shown in Fig. 2.10. This vehicle essentially consists of a raked cone followed by a circular cylinder. It is a fairly complicated shape in that it is a combination of several bodies. It has sharp corners and a concave region. The inner and outer boundaries are generated as follows.

Inner Boundary:

Inner boundary is constructed with respect to the axes ox and oy in Fig. 2.10. BCD is an arc of an ellipse

$\frac{x^2}{r_1^2} + \frac{y^2}{r_2^2} = 1$ with $r_1 = 1.0$ units and $r_2 = 0.6$ units with centre at O. The coordinates (x_A, y_A) of the point A, where the raked surface cuts the x-axis is given by $(-0.6, 0.0)$. The equation of a straight line which passes through the point A and makes an angle θ with the x-axis is given by $y = m(\theta) (x - x_A)$ where $m(\theta) = \tan \theta$. The intersection of this line with the prescribed value of θ ($\theta = \theta_0 = 70^\circ$ or 90°), with the ellipse gives the points B and D. The x value of the points B and D is given by

$$x = \frac{r_1^2 |m(\theta)|^2 x_A}{r_2^2 + r_1^2 |m(\theta)|^2} \pm \sqrt{\frac{r_2^2 + |m(\theta)|^2 (r_1^2 - x_A^2)}{r_2^2 + r_1^2 |m(\theta)|^2} r_1 r_2}$$

with the (+) sign for B and (-) sign for D. These values of x are substituted in the equation of the straight line to get the corresponding value of y.

$$\text{Now, } \bar{AA}' = r_2 \sqrt{1 - \frac{x_A^2}{r_1^2}}$$

The equation of the line \overline{HG} is $y = 0.2 x \bar{AA}'$ and the intersection of this line with \overline{AB} gives the point H.

$$\therefore y_H = 0.2 x \bar{AA}'$$

$$x_H = y_H / m(\theta_0) + x_A$$

Another line \overline{EF} , $y = -0.2 \times \overline{AA}$ is also drawn and the intersection of this line with \overline{AD} gives the point E.

$$y_E = -0.2 \times \overline{AA}$$

$$x_E = y_E/m(O_O) + x_A$$

The intersections of the line $x = 0$ with the lines $y = y_H$ and $y = y_E$ gives the coordinates of the point G and F respectively. Thus, $x_G = 0.0$, $y_G = y_H$, $x_F = 0.0$ and $y_F = y_E$.

It is decided to distribute $N_1 (= 4)$, $N_2 (= 8)$, $N_3 = (5)$ $N_4 (= 9)$, $N_5 (= 5)$, $N_6 (= 8)$ and $N_7 (= 3)$ grid points on the segments \overline{OG} , \overline{GH} , \overline{HB} , \overline{BCD} , \overline{DE} , \overline{EF} and \overline{FO} respectively. The following convention is introduced here to make the discussion simpler and easier to understand. $N_{12} = N_1 + N_2$, $N_{13} = N_1 + N_2 + N_3$ and so on and $N_{17} = N_1 + N_2 + \dots + N_7$. Thus point O is the first grid point, point G is the N_1^{th} grid point, point H is the N_{12}^{th} grid point, and so on, and point F is the N_{16}^{th} grid point and again point O is the N_{17}^{th} grid point.

The quantities Δy_G , Δx_H and Δx_F are defined as follows:

$$\Delta y_G = \overline{OG}/(N_1 - 1)$$

$$\Delta x_H = \overline{GH}/N_2$$

$$\Delta x_F = \overline{EF}/N_6$$

They will be used while defining the boundary conditions.

Outer Boundary:

Outer boundary is constructed with respect to the $XO''Y$ axes.

The outer boundary consists of a parabola IKM and a straight line \overline{IM} . The equation of the parabola is given by

$$y^2 = ax + c \quad (2.15)$$

The values of the constant a and c are found by specifying two points K and J on the parabola. The coordinate (x_k, y_k) of the point K is $(0.5, 0)$ which gives from equation (2.15) $c = -ax_k$. Coordinate (x_J, y_J) of the point J is prescribed as follows:

$$x_J = x_B$$

$$y_J = y_B + \overline{BJ}$$

\overline{BJ} is perpendicular to x -axis and is assigned a value 0.6. Substituting the values of x_J , y_J and c in equation (2.15) the value of a is found to be

$$a = y_J^2 / (x_J - x_K)$$

To distribute the grid points, the outer boundary is divided into segments $\overline{O'I}$, $\overline{IJ'}$, $\overline{JK'}$, \overline{KL} , \overline{LM} and \overline{MO} . The points J' and L are obtained by the intersection of a straight line, making an angle 80° with the x -axis and passing through the point A , with the parabola.

The x-coordinates of the points J' and L is given by

$$x = \left(\frac{a}{2|m(\theta)|^2} + x_A \right) \pm \sqrt{\left(\frac{a^2 + 4|m(\theta)|^2(c+a x_A)}{2|m(\theta)|^2} \right)}$$

+ sign is taken for the point J' and -sign for the point L.

Corresponding Y values are found from the equation

$$y = m(\theta) (x - x_A).$$

The number of points that are distributed on the segments \overline{OI} , $\overline{IJ'}$, $\overline{JK'}$, \overline{LM} and $\overline{MO'}$ are $M_1 (=8)$, $M_2 (=9)$, $M_3 (=N_4 = 9)$, $M_4 (=9)$ and $M_5 (=7)$ respectively. Thus, point O' is the first grid point, I is the M_1^{th} grid point, J' is the M_12^{th} grid point, L is the M_{13}^{th} grid point M is the M_{14}^{th} grid point and again O' is the M_{15}^{th} grid point. The quantities Δy_I , $\Delta x_{J'}$, Δx_L are defined as follows and are used while defining the boundary conditions.

$$\Delta y_I = y_I / (M_1 - 1)$$

$$\Delta x_{J'} = (x_{O'} - x_{J'}) / M_2$$

$$\Delta x_L = (x_{O'} - x_L) / M_4$$

Boundary Conditions:

The distance $\bar{K}\bar{C}$ in Fig. (2.10) is defined to be 0.5. This makes the transformation relationship between (x, y) -axes and (X, Y) -axes to be

$$X = x + \overline{O\bar{O}} = x + 2.0$$

$$Y = y.$$

The boundary conditions on the inner and outer boundaries are defined with respect to (X, Y) -axes and the subsequent generation of the grids is also with respect to (X, Y) -axes only.

(i) Inner boundary i.e. $\eta = 1$

(a) Segment \overline{OG} .

$$x_{i,1} = 2.0 \text{ with } \xi_i = i = 1, 2, \dots, N1$$

$$y_{i,1} = (i-1)\Delta y_G \text{ with } \xi_i = i = 1, 2, \dots, N1$$

(b) Segment \overline{GH} .

$$x_{i,1} = (i-N1) \Delta x_H \text{ with } \xi_i = i = N1+1, \dots, N12$$

$$y_{i,1} = y_{N1} \text{ with } \xi_i = i = N1+1, \dots, N12$$

(c) Segment \overline{HB}

$$x_{i,1} = \frac{(i-N12)x_B + (N13-i)x_H}{(N3-1)} \text{ with } \xi_i = i = N12+1, \dots, N13$$

$$Y_{i,1} = \frac{(i-N12)Y_B + (N13-i)Y_H}{(N3-1)} \quad \text{with } \xi_i = i = N12+1, \dots, N13$$

(d) Segment \overbrace{BCD}

$$\theta_i = \theta_0 + (i-N13) \Delta\theta \text{ where } \Delta\theta = 20^\circ$$

$$x_{i,1} = \frac{r_1^2 + |m(\theta_i)|^2 x_A}{r_2^2 + r_1^2 |m(\theta_i)|^2} \pm \frac{r_1 r_2 \sqrt{r_2^2 + |m(\theta_i)|^2 (r_1^2 - x_A^2)}}{r_2^2 + r_1^2 |m(\theta_i)|^2}$$

$$\text{with } \xi_i = i = N13+1, \dots, N14$$

-ve sign is taken if $\pi/2 \leq \theta_i \leq 3\pi/2$ and +ve sign is taken otherwise.

$$Y_{i,1} = M(\theta_i)(x_{i,1} - x_A) \text{ with } \xi_i = i = N13+1, \dots, N14$$

(e) Segment \overline{DE} .

$$x_{i,1} = \frac{(i - N13)x_E + (N14-i)x_H}{(N5-1)} \quad \text{with } \xi_i = i = N14+1, \dots, N15$$

$$Y_{i,1} = \frac{(i - N13)Y_E + (N14-i)Y_H}{(N5-1)} \quad \text{with } \xi_i = i = N14+1, \dots, N15$$

(f) Segment \overline{EF} .

$$x_{i,1} = (i-N15) \Delta x_F \quad \text{with } \xi_i = i = N15+1, \dots, N16$$

$$Y_{i,1} = Y_{N15} \quad \text{with } \xi_i = i = N15+1, \dots, N16$$

(g) Segment \overline{FO} .

$$x_{i,1} = x_{N16} \text{ with } \xi_i = i = N16+1 \dots N17$$

$$y_{i,1} = (i-N16) \Delta y_G \text{ with } \xi_i = i = N16+1 \dots N17$$

(ii) Outer Boundary i.e. = J.

(a) Segment O I.

$$x_{i,J} = x_O = 4.0 \text{ with } \xi_i = i = 1 \dots M1$$

$$y_{i,j} = (i-1) \Delta y_I \text{ with } \xi_i = i = 1 \dots M1$$

(b) Segment IJ

$$x_{i,J} = (i-M1) \Delta x_J \text{ with } \xi_i = M1+1, \dots, M12-1$$

$$y_{i,J} = \sqrt{a x_{i,J} + c} \text{ with } \xi_i = M1+1, \dots, M12-1.$$

(c) Segment J' KL.

$$\theta_i = 80^\circ + (i-M12) \Delta \theta \text{ where } \Delta \theta = 20^\circ$$

$$x_{i,J} = \left(\frac{a}{2|m(\theta_i)|^2} + x_A \right) \pm \left(\frac{\sqrt{a^2 + 4|m(\theta_i)|^2(c+a x_A)}}{2|m(\theta_i)|^2} \right)$$

$$\text{with } \xi_i = i = M12, \dots, M13$$

(-) sign is taken if $\pi/2 \leq \theta_i \leq 3\pi/2$ and (+) sign is taken otherwise.

$$Y_{i,J} = m(\theta_i) (X_{i,J} - X_A) \text{ with } \xi_i = i = M12, \dots, M13$$

(d) Segment LM.

$$X_{i,J} = (i-M13) \Delta X_M \text{ with } \xi_i = i = M13+1, \dots, M14$$

$$Y_{i,J} = -\sqrt{a X_{i,J} + c} \text{ with } \xi_i = i + M13+1, \dots, M14$$

(e) Segment MO.

$$X_{i,J} = X_{i,M14} \text{ with } \xi_i = i = M14+1, \dots, M15$$

$$Y_{i,J} = (i-M14) \Delta Y_I \text{ with } \xi_i = i = M14+1, \dots, M15.$$

Initial Grid and Solution Procedure:

Points $(x_{i,1}, y_{i,1})$ on the inner boundary are joined to points $(x_{i,J}, y_{i,J})$ on the outer boundary, with $J = 36$, by straight lines. These are the constant- ξ lines. Each constant- ξ line is divided into $(J-1)$ equal parts and the constant- η lines are constructed as described in the last example. Using this grid, SAR method is used to solve the Poisson equations (2.10) with $P = 0$ and the following cases of Q :

(i) $Q = 0$. This gives Laplace equations.

(ii) Q as given by equation (2.12b) with $b_1 = 10.0$ and $d_1 = 0.025$. Constant- η lines are to be attracted to the point H in Fig. (2.10).

Discussion of the Results:

The initial grid, solution of Laplace equations and solution of Poisson equations around the AFE vehicle are shown in Figs. (2.11), (2.12), and (2.13) respectively. In these figures and in Fig. (2.10) the outer boundary IKM (Fig. 2.10) is a parabola. But there seems to be a sharp corner at point K. This is due to the fact that the adjacent grid points are connected by straight lines, instead of smooth lines, by the computer.

It could be seen that a marked difference exists between the initial grid and the other two. The grid lines are smooth in both the cases of Laplace solution and Poisson solution. In both the Figs. (2.12) and (2.13) grid points are concentrated near the surface where the gradients of the flow variables are supposed to be large and sparsely distributed away from the surface.

Comparing Figs. (2.12) and (2.13) it could be seen that the first constant- η line away from the inner body is almost the same in both the cases but other constant- η

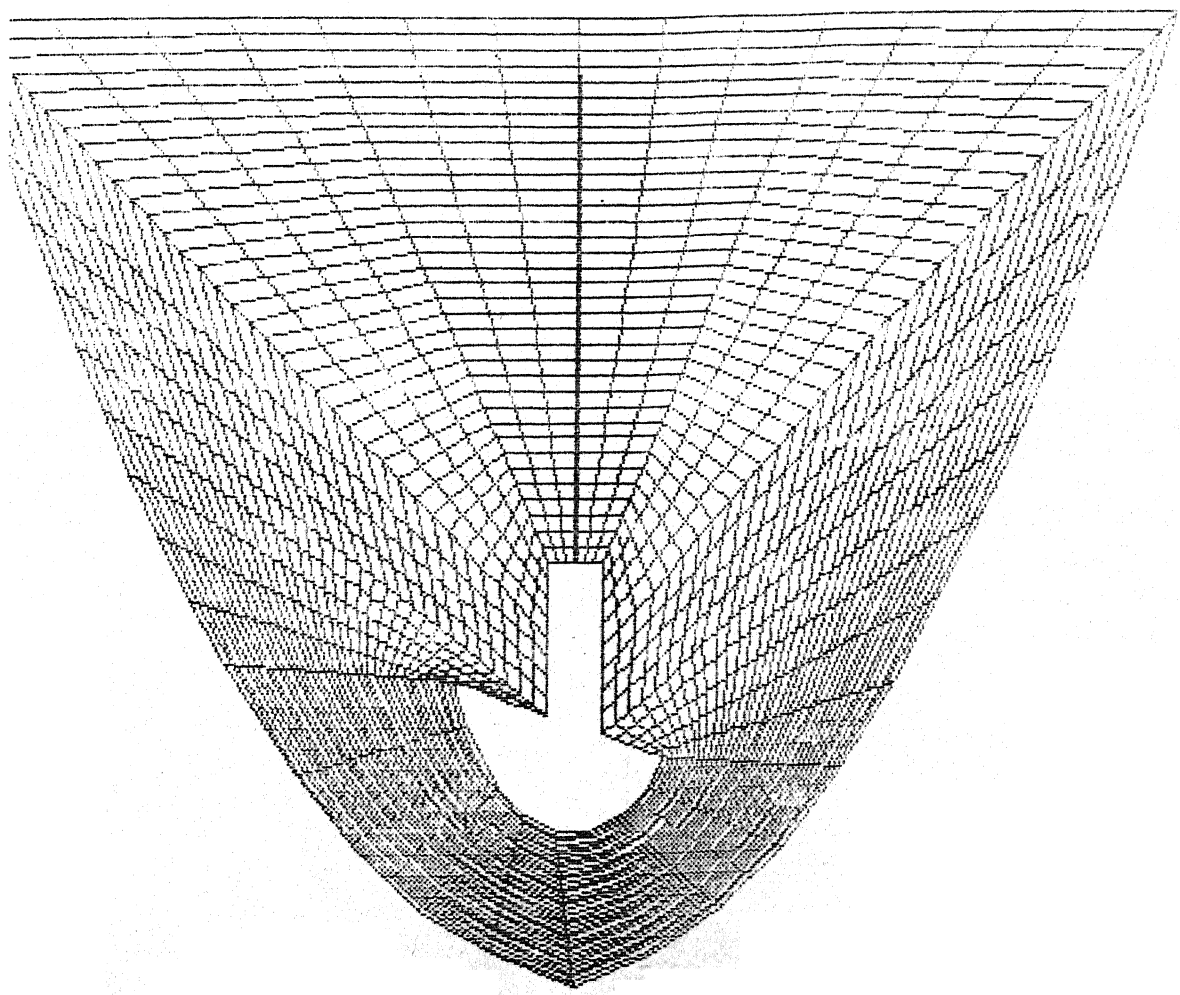
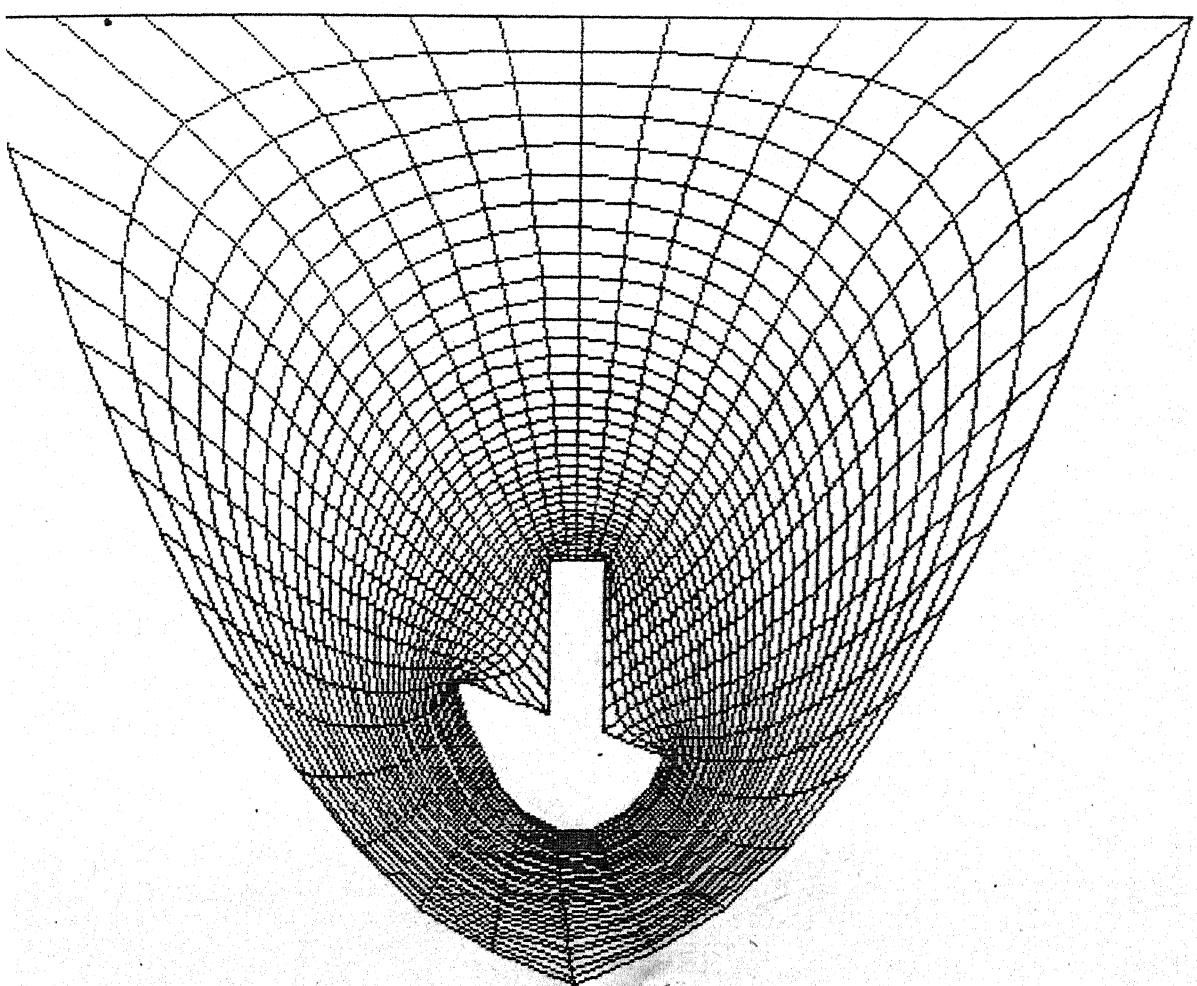


FIGURE 2.11 Aero-Assisted Flight Experiment

FIGURE 2.12 Aero-Assisted Flight Experiment Vehicle-Laplace Solution



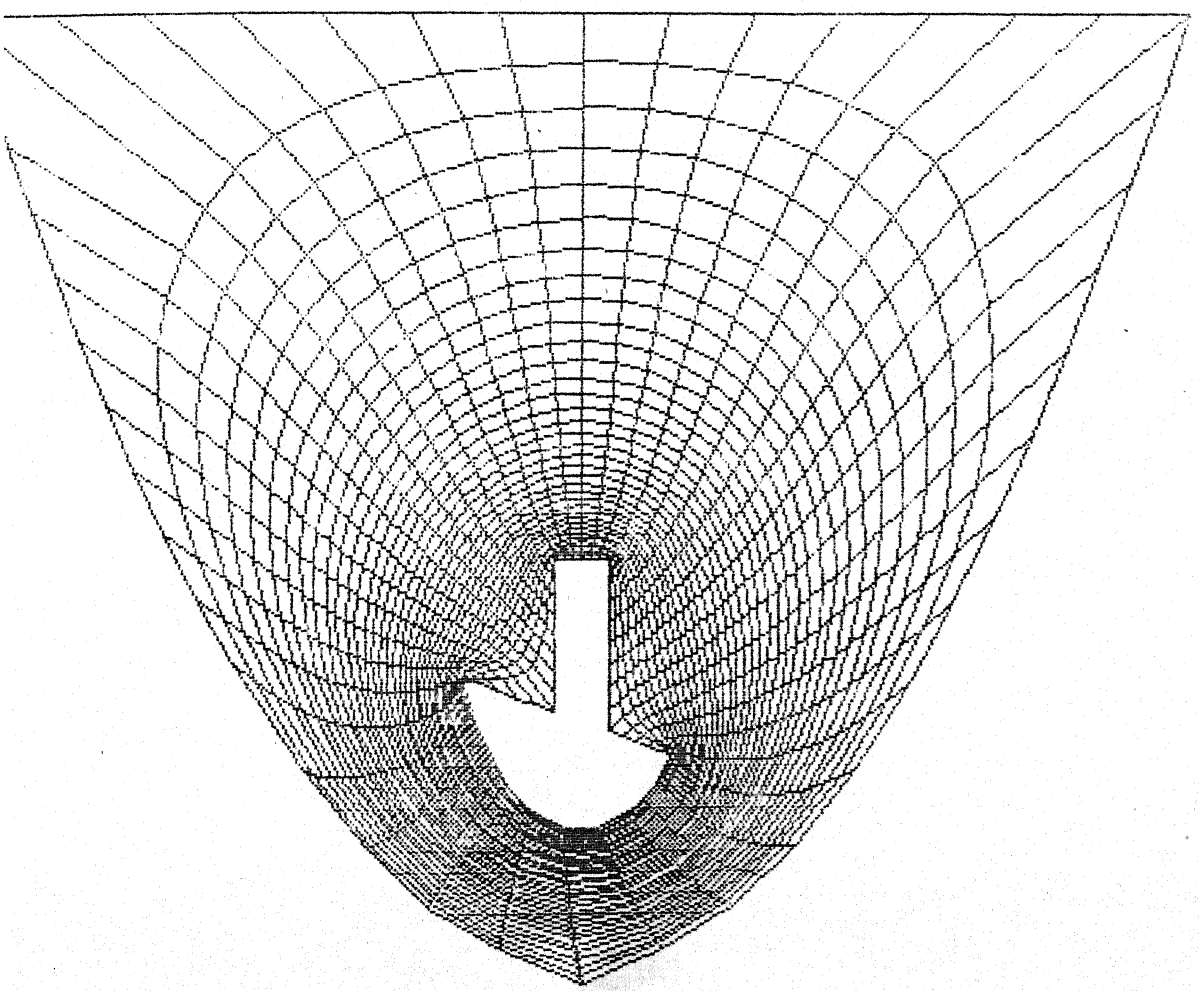


FIGURE 2.13 Aero-Assisted Flight Experiment Vehicle-Poisson Solution

lines are attracted towards the point H, as seen in Fig. (2.13). The inability of the first constant- η line away from the inner body to move closer to the inner body, in the region near the point H, may be due to the sharp concave corner at point H of the inner body or due to the fact that the choice of the control function Q in Poisson equation (2.12b) needs further modification by numerical experiments. More constant- η lines can be attracted towards the point H, either by taking a smoothly varying concave surface around the point H, instead of the present sharp corner, or by making the control functions P and Q in the Poisson equations (2.11) dependent on the flow variables which are obtained as the solutions of the governing equations. For similar reasons, it is observed that there are few grid points near the concave corners I and M of the outer boundary.

CHAPTER 3ADAPTATIVE GRID GENERATION TECHNIQUE3.1 Description

In Chapter 2, the problem of errors arising due to inaccurate representation of the boundaries of bodies of arbitrary shapes was addressed to, by developing a body-fitted coordinate system. In the present chapter, the problem of errors, in the numerical solution of flow fields, arising due to inaccurate resolution of the gradients and/or curvatures of the flow profiles is addressed to. Generally, such large gradients and/or curvatures occur near the surface and in certain cases they in addition occur somewhere in the flow field whose location is not known a priori. These gradients and/or curvatures of the flow profiles can be resolved properly by moving more number of grid points to regions where gradients and/or curvatures are large from regions where they are small. In an iterative procedure of solving the flow problem, the grids are moved to desired location as the solution develops from some initial state.

As mentioned in the last chapter one way of moving the grid points is to make the control functions P and Q dependent on the gradients and/or curvatures. But this approach is not quite attractive because it is an indirect

way of moving the grid points and it is very difficult to choose the particular form of the control functions which will move the points to the desired locations.

A more direct method would be to relate the gradients and/or curvatures of the solutions of the flow problem to the grid intervals in the physical domain in such a way that the grid intervals become small at locations of large gradients and/or curvatures. Such a method of moving the grid points is called the adaptive grid technique.

Since the grid points in the physical domain are moved, the grid intervals become uneven and the coordinate lines may become non-orthogonal. For these reasons the physical domain is again transformed to the computational rectangular domain as in the last chapter. The initial transformation is fixed numerically in most of the cases.

In the present investigation adaptive grid technique is applied to a one-dimensional problem. The physical coordinate is represented by η and the computational coordinate is by ξ . Both η and ξ vary from zero to unity with the grid size in the computational domain being $\Delta\xi = 1/NDIV$ where $NDIV$ is the total number of grid intervals. The grids in the physical plane are moved depending on gradients and curvatures or gradients alone.

3.2 Mathematical Development

As shown by Brockbill and Saltzmann⁷, for one-dimensional adaptation, the total error is reduced when the grid points are distributed such that

$$\int_{x_i}^{x_{i+1}} w(x) dx = \text{constant} \quad (3.1)$$

for all i , where $w(x)$ is a positive weight function.

Usually the gradients of the evolving solution are taken as the weight function as they are related to the error in the solution.

To maintain a uniform grid in the ξ -space equation (3.1) implies that

$$x_\xi w(\xi) = \text{constant} \quad (3.2)$$

where x_ξ is the metric coefficient and corresponds to the ratio of arc lengths in the physical and computational space. But equation (3.2) is also the Euler-Lagrange equation for minimising the integral

$$I_w = \int_0^1 w(\xi) x_\xi^2 d\xi \quad (3.3)$$

physically the minimisation of the above integral represents the minimisation of the energy of a system of tension springs with spring constants $w(\xi)$ between each pair of grid points. The constant in equation (3.2) is evaluated according to Nakahashi and Deiwert¹⁴ as follows.

Let the constant be denoted by c . Rewriting equation (3.2),

$$dx_i = \frac{c d \xi}{w(\xi)} \quad (3.4)$$

Integrating over all the grid intervals,

$$\int_0^L dx_i = c \int_0^1 \frac{d\xi}{w(\xi)}$$

$$\text{i.e. } L = c \int_0^1 \frac{d\xi}{w(\xi)} \quad (3.5)$$

where L is the total length in the physical plane.

Rewriting equation (3.5),

$$c = L / \int_0^1 \frac{d\xi}{w(\xi)} \quad (3.6)$$

Also, if there are N grid intervals then $N d\xi = 1$,

$$\text{which implies } d\xi = \frac{1}{N} \quad (3.7)$$

Putting (3.6) and (3.7) in (3.4),

$$dx_i = L / [N w(\xi_i) \int_0^1 \frac{d\xi}{w(\xi_i)}] \quad (3.8)$$

$$\text{or } \Delta x_i = L / [w(\xi_i) \sum_{i=1}^N \frac{1}{w(\xi_i)}]$$

Equation (3.8) is the equation used in this work for grid adaptation. The form of the weight function is taken as

$$w(\xi_i) = 1 + A \left| \frac{df}{d\xi} \right|_i + B \left| \frac{d^2 f}{d\xi^2} \right|_i \quad (3.9)$$

with A to be one in all cases and B varying from 0 to 0.4. f is chosen to be a combination of temperature and normal component of velocity. The reasons for choosing this particular combination of the dependent variable in the weight function are stated in the section entitled "choice of the dependent variable in the weight function w" in Chapter 4.

CHAPTER 4HYPersonic MERGED LAYER FLOW NEAR THE STAGNATION POINT OF A BLUNT BODY4.1 Introduction

When a space vehicle reenters the atmosphere at about 120 km altitude, its velocity is of the order of 6 to 10 km/s. The ambient conditions are (i) the density of the order 10^{-9} kg/m³ and the molecular mean free path of the order of 1m.

The boundary layer thickness is inversely proportional to the square-root of Reynolds number and the shock thickness is directly proportional to the freestream molecular mean free path. The Reynolds number is very small since the density is very small even though the flight speed is large. This means that the thickness of the boundary layer is very large and therefore boundary layer approximations are not valid. The shock wave is very thick since the mean free path is large and therefore Rankine-Hugoniot relations are not valid. Moreover owing to their large thicknesses both the viscous region near the surface and the shock wave like region merge into each other and this makes the entire disturbed zone viscous. The whole disturbed zone is called the merged layer.

Particles moving in the merged layer do not suffer enough collisions with other particles and by the time they reach

the body, they retain enough momentum to slide over the body with a finite velocity. This velocity is called the slip velocity. Similarly the temperature at the base of the viscous layer is different from that of the body. This is called the temperature jump. Using kinetic theory approach, the expression for velocity and temperature jump are given by Kennard³¹ as follows:

$$u_b \propto \lambda_b \left(\frac{\partial u}{\partial y} \right)_b$$

$$(T_b - T_w) \propto \lambda_b \left(\frac{\partial T}{\partial y} \right)_b$$

where u and T are the tangential component of velocity and temperature respectively and y is the coordinate normal to the body. The subscripts b and w denote the base of the viscous layer and the wall respectively. λ is the mean free path.

The flow in the merged layer is described by the full Navier-Stokes equations. Local similar solutions valid in the stagnation zone of a spherical surface have been obtained. The resulting equations are integrated from the surface, with slip and temperature jump conditions, to the free stream so as to catch the shock wave like structure in the outer region as part of the computational domain.

Merged layer problem has been extensively analysed and studied by Jain¹⁶⁻¹⁹, Jain and Adimurthi²⁰⁻²², Kumar and Jain^{23,24}, Jain and Kumar²⁵, Jain and Saroj Prabha^{26,27}, Jain and Woods²⁸ and Singh and Jain²⁹, using full Navier-Stokes

equations with slip and temperature jump surface conditions, on uniform grids.

In the present investigations, computations have been carried out with uniform and adapted grids for shuttle flight conditions. It had been found that with adaptation (i) the accuracy of the results increased, (ii) the range of applicability of the merged layer approach had been extended to a higher range of Reynolds number and (iii) the computer time was saved.

4.2 Mathematical Development

The full Navier-Stokes equations in spherical polar coordinates, with axial symmetry are the following:

Continuity equation:

$$(\rho v)_r + \frac{2\rho v}{r} + \frac{\rho u}{r} + \frac{\rho u \cot\theta}{r} = 0 \quad (4.1)$$

Radial momentum equation:

$$\begin{aligned} p_r + \rho(v v_r + \frac{u}{r} v_\theta - \frac{u^2}{r}) \\ = 2[\mu v_r - \frac{1}{3r} (r v_r + 2v + u_\theta + u \cot\theta)]_r \\ + \frac{1}{r} \{\mu [r (\frac{u}{r})_r + \frac{v_\theta}{r}]\}_\theta + \frac{2\mu}{r} (2v_r - \frac{u \cot\theta}{r}) \\ + \frac{\mu}{r} \{\cot\theta [r (\frac{u}{r})_r + \frac{v_\theta}{r}]\} - \frac{2}{r} (v + u \cot\theta) \end{aligned} \quad (4.2)$$

Transverse momentum equation:

$$\begin{aligned}
 \frac{p_\theta}{r} + \rho(v u_r + \frac{u}{r} u_\theta + \frac{uv}{r}) \\
 = \frac{2}{r} \left[\frac{\mu}{r} (u_\theta + v) - \frac{\mu}{3r} (r v_r + 2v + u_\theta + u \operatorname{Cot}\theta) \right]_\theta \\
 + \left\{ \mu \left[r \left(\frac{u}{r} \right)_r + \frac{v_\theta}{r} \right] \right\}_r + \frac{3\mu}{r} \left[r \left(\frac{u}{r} \right)_r + \frac{v_\theta}{r} \right] \\
 + \frac{2\mu}{r^2} \operatorname{Cot}\theta (u_\theta - u \operatorname{Cot}\theta) \tag{4.3}
 \end{aligned}$$

Energy equation:

$$\begin{aligned}
 \rho (v h_r + \frac{u}{r} h_\theta) = v p_r + \frac{u}{r} p_\theta + \frac{1}{r p_r} \left[\mu_r r h_r \right]_r + \frac{\mu}{r} h_\theta + \mu h_r + \mu h_\theta \frac{\operatorname{Cot}\theta}{r} \\
 + \mu \left[2 \frac{v_r^2}{r^2} + \frac{2}{r^2} (u_\theta + v)^2 + \frac{2}{r^2} (v + u \operatorname{Cot}\theta)^2 + \left(r \left(\frac{u}{r} \right)_r + \frac{v_\theta}{r} \right)^2 \right] \\
 - \frac{2\mu}{3r^2} [r v_r + v_\theta + 2v + u \operatorname{Cot}\theta]^2 \tag{4.4}
 \end{aligned}$$

Equation of state:

$$p = \rho RT \tag{4.5}$$

Viscosity-temperature relation:

$$\mu \propto \sqrt{T} \tag{4.6}$$

Here, r and θ represent the radial distance and vectorial angle respectively (See Fig. 4.1); u and v are the velocity components in increasing r and θ directions respectively; ρ , p and h are the density, pressure and specific enthalpy respectively; μ is the coefficient of viscosity; R is the gas constant; Pr is the Prandtl number; C_p is the specific heat at constant pressure and γ is the ratio of specific heats. Suffixes r and θ - denote the derivatives of the dependent variables with respect to ' r ' and ' θ ' respectively.

Boundary conditions are:

At the outer edge of the merged layer, $r = r_e$

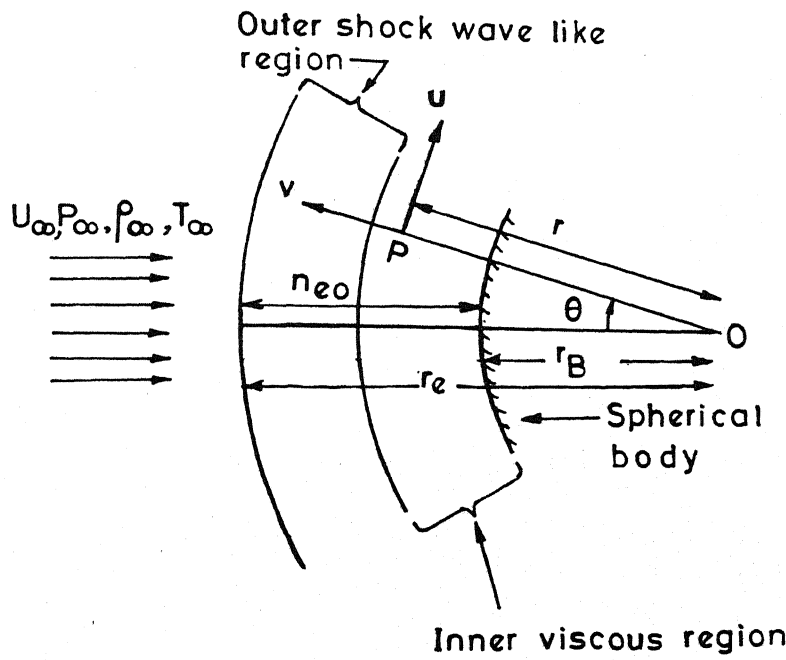
$$\begin{aligned}
 u &= V_\infty \sin\theta \\
 v &= -V_\infty \cos\theta \\
 p &= p_\infty \\
 \rho &= \rho_\infty \\
 T &= T_\infty
 \end{aligned} \tag{4.7}$$

At the surface of the body, $r = r_B$, slip velocity and temperature jump boundary conditions are

$$u = \frac{2-\sigma}{\sigma} \sqrt{\frac{\pi\gamma}{2}} \left[\frac{\mu}{\rho a} \left(\frac{\partial u}{\partial r} \right) \right]_{r_B}, v = 0 \tag{4.8a,b}$$

$$T = T_w + \left(\frac{2-\alpha}{\alpha} \right) \left(\frac{2\gamma}{\gamma+1} \right) \sqrt{\frac{\pi\gamma}{2}} \left[\frac{\mu}{Pr \rho a} \left(\frac{\partial T}{\partial r} \right) \right]_{r_B} \tag{4.9}$$

where σ and α are the momentum and thermal accommodation coefficients and T_w is the prescribed wall temperature.



ρ, p, T = Density, Pressure and Temperature respectively

v, u = Velocity components in r, θ direction respectively

μ = Viscosity

Subscript ' ∞ ' denotes freestream conditions

FIG. 4.1

For the adiabatic wall case,

$$\left(\frac{\partial T}{\partial r}\right)_{r_B} = 0 \quad (4.10)$$

For the noslip conditions, at $r = r_B$,

$$u = v = 0; T = T_w \quad \text{or} \quad \left(\frac{\partial T}{\partial r}\right) = 0$$

Non-dimensionalization Procedure

The non-dimensional variables are defined as follows:

$$\bar{u} = \frac{u}{v_\infty}, \quad \bar{v} = \frac{v}{v_\infty}, \quad \bar{p} = \frac{p}{\rho_\infty v_\infty^2}, \quad \bar{\rho} = \frac{\rho}{\rho_\infty},$$

$$\bar{T} = \frac{T}{T_{\infty}}, \quad \bar{\mu} = \frac{\mu}{\mu_\infty}, \quad \bar{r} = \frac{r}{r_B}, \quad \text{Re}_\infty = \frac{v_\infty r_B \rho_\infty}{\mu (T_{\infty})}$$

where the suffix ' ∞ ' denotes the value of the variable at the freestream location and T_{∞} is the freestream stagnation temperature.

The governing equations (4.1) to (4.6) and the boundary conditions (4.7) to (4.10) in the non-dimensional form become

$$\left(\bar{\rho} \bar{v}\right)_{\bar{r}} + \frac{2 \bar{\rho} \bar{v}}{\bar{r}} + \frac{(\bar{\rho} \bar{u})_{\theta+}}{\bar{r}} + \frac{\bar{\rho} \bar{u} \cot \theta}{\bar{r}} = 0 \quad (4.11)$$

$$\begin{aligned}
\frac{\bar{p}_r}{r} + \bar{\rho} \left(\bar{v} \bar{v} \frac{1}{r} \right) + \frac{\bar{u}}{r} \bar{v}_\theta - \frac{\bar{u}^2}{r} \\
= \frac{2}{Re_O} \left[\bar{\mu} \bar{v} \frac{1}{r} - \frac{\bar{\mu}}{3r} \left(\bar{r} \bar{v} \frac{1}{r} + 2\bar{v} + \bar{u}_\theta + \bar{u} \cot\theta \right) \right] \frac{1}{r} \\
+ \frac{1}{Re_O \bar{r}} \left\{ \bar{\mu} \left[\bar{r} \left(\frac{\bar{u}}{r} \right) \frac{1}{r} + \frac{\bar{v}_\theta}{r} \right] \right\}_\theta + \frac{2\bar{\mu}}{Re_O \bar{r}} \left(2\bar{v} \frac{1}{r} - \frac{\bar{u}_\theta + v}{r} \right) \\
+ \frac{\bar{\mu}}{Re_O \bar{r}} \left\{ \cot\theta \left[\bar{r} \left(\frac{\bar{u}}{r} \right) \frac{1}{r} + \frac{\bar{v}_\theta}{r} \right] - \frac{2}{r} (\bar{v} + \bar{u} \cot\theta) \right\} \\
(4.12)
\end{aligned}$$

$$\begin{aligned}
\frac{\bar{p}_\theta}{r} + \bar{\rho} \left(\bar{v} \bar{u} \frac{1}{r} + \frac{\bar{u}}{r} \bar{u}_\theta + \frac{\bar{u} \bar{v}}{r} \right) \\
= \frac{2}{Re_O \bar{r}} \left[\frac{\bar{\mu}}{r} (\bar{u}_\theta + \bar{v}) - \frac{\bar{\mu}}{3r} \left(\bar{r} \bar{v} \frac{1}{r} + 2\bar{v} + \bar{u}_\theta + \bar{u} \cot\theta \right) \right]_\theta \\
+ \frac{1}{Re_O} \left\{ \bar{\mu} \left[\bar{r} \left(\frac{\bar{u}}{r} \right) \frac{1}{r} + \frac{\bar{v}_\theta}{r} \right] \right\} \bar{r} + \frac{3\bar{\mu}}{Re_O \bar{r}} \left[\bar{r} \left(\frac{\bar{u}}{r} \right) \frac{1}{r} + \frac{\bar{v}_\theta}{r} \right] \\
+ \frac{2\bar{\mu}}{Re_O \bar{r}^2} \cot\theta (\bar{u}_\theta - \bar{u} \cot\theta) \\
(4.13)
\end{aligned}$$

$$\rho \left[\Lambda \left(\bar{v} \frac{\bar{T}}{\bar{r}} + \frac{\bar{u}}{\bar{r}} \bar{T}_\theta \right) \right] = \bar{v} \frac{\bar{p}}{\bar{r}} + \frac{\bar{u} \bar{p}_\theta}{\bar{r}}$$

$$+ \frac{1}{Pr} \frac{1}{Re_O} \frac{\Lambda}{\bar{r}} \left\{ \left(\bar{\mu} \bar{r} \frac{\bar{T}}{\bar{r}} \right) \frac{1}{\bar{r}} + \frac{\bar{\mu} \bar{T}_\theta}{\bar{r}} + \bar{\mu} \frac{\bar{T}}{\bar{r}} + \frac{\bar{\mu} \bar{T}_\theta}{\bar{r}} \cot\theta \right\}$$

$$+ \frac{1}{Re_O} \bar{\mu} \left[2 \bar{v} \frac{2}{\bar{r}} + \frac{2}{\bar{r}^2} (\bar{u}_\theta + \bar{v})^2 + \frac{2}{\bar{r}^2} (\bar{v} + \bar{u} \cot\theta)^2 + \left[\bar{r} \left(\frac{\bar{u}}{\bar{r}} \right) \frac{1}{\bar{r}} + \frac{\bar{v}_\theta}{\bar{r}} \right]^2 \right]$$

$$- \frac{2 \bar{\mu}}{3 Re_O \bar{r}^2} \left[\bar{r} \bar{v} \frac{1}{\bar{r}} + \bar{v}_\theta + 2 \bar{v} + \bar{u} \cot\theta \right]^2 \quad (4.14)$$

$$\bar{p} = \frac{\gamma - 1}{\gamma} \Lambda \bar{\rho} \bar{T} \quad (4.15)$$

$$\bar{\mu} = \sqrt{\bar{T}} \quad (4.16)$$

where

$$\Lambda = \frac{C_p T_\infty}{v_\infty^2} = \frac{1}{2} + \frac{1}{(\gamma - 1) M_\infty^2} \quad (4.17)$$

Here, C_p , γ and Pr are treated as constants.

Boundary conditions are:

$$\text{At } \bar{r} = \bar{r}_e$$

$$\bar{u} = \sin\theta$$

$$\bar{v} = -\cos\theta$$

$$\bar{\rho} = 1; \bar{T} = 1 - \frac{1}{2\Lambda}; \bar{p} = \frac{1}{\gamma M_\infty^2} \quad (4.18)$$

$$\bar{\rho} \left[\Lambda \left(\bar{v} \frac{\bar{T}}{\bar{r}} + \frac{\bar{u}}{\bar{r}} \bar{T}_\theta \right) \right] = \bar{v} \frac{\bar{p}}{\bar{r}} + \frac{\bar{u} \bar{p}_\theta}{\bar{r}}$$

$$+ \frac{1}{Pr} \frac{1}{Re_\infty} \frac{\Lambda}{\bar{r}} \left\{ \left(\bar{\mu} \frac{\bar{T}}{\bar{r}} \right) \frac{\bar{T}}{\bar{r}} + \frac{\bar{\mu} \bar{T}_\theta}{\bar{r}} + \bar{u} \bar{T} \frac{\bar{T}}{\bar{r}} + \frac{\bar{\mu} \bar{T}_\theta}{\bar{r}} \cot\theta \right\}$$

$$+ \frac{1}{Re_\infty} \bar{\mu} \left[2\bar{v}^2 + \frac{2}{\bar{r}^2} (\bar{u}_\theta + \bar{v})^2 + \frac{2}{\bar{r}^2} (\bar{v} + \bar{u} \cot\theta)^2 + \left[\bar{r} \left(\frac{\bar{u}}{\bar{r}} \right) \frac{\bar{v}}{\bar{r}} + \frac{\bar{v}_\theta}{\bar{r}} \right] \right]$$

$$- \frac{2 \bar{\mu}}{3Re_\infty \bar{r}^2} \left| \bar{r} \bar{v} \frac{\bar{v}}{\bar{r}} + \bar{u}_\theta + 2\bar{v} + \bar{u} \cot\theta \right|^2 \quad (4.14)$$

$$\bar{p} = \frac{\gamma - 1}{\gamma} \Lambda \bar{\rho} \bar{T} \quad (4.15)$$

$$\bar{\mu} = \sqrt{\bar{T}} \quad (4.16)$$

where

$$\Lambda = \frac{C_p T_\infty}{V_\infty^2} = \frac{1}{2} + \frac{1}{(\gamma - 1) M_\infty^2} \quad (4.17)$$

Here, C_p , γ and Pr are treated as constants.

Boundary conditions are:

$$\text{At } \bar{r} = \bar{r}_e$$

$$\bar{u} = \sin\theta$$

$$\bar{v} = -\cos\theta$$

$$\bar{\rho} = 1; \bar{T} = 1 - \frac{1}{2\Lambda}, \bar{p} = \frac{1}{\gamma M_\infty^2} \quad (4.18)$$

At $\bar{r} = 1$

Slip velocity is

$$\bar{u} = \sqrt{\frac{\pi\gamma}{2}} \left(\frac{2-\sigma}{\sigma} \right) \frac{M_\infty}{Re_O} \sqrt{\frac{T_\infty}{T_{O^\infty}}} \left(\frac{\bar{\mu}}{\bar{\rho}\sqrt{T}} \right) \left. \frac{\partial \bar{u}}{\partial \bar{r}} \right|_{\bar{r}=1} \quad (4.19)$$

and

$$\bar{v} = 0 \quad (4.20)$$

Temperature jump conditions is

$$\bar{T} = \bar{T}_w + \left(\frac{2-\alpha}{\alpha} \right) \left(\frac{2\gamma}{\gamma+1} \right) \sqrt{\frac{\pi\gamma}{2}} \frac{M_\infty}{Pr Re_O} \sqrt{\frac{T_\infty}{T_{O^\infty}}} \left. \frac{\bar{\mu}}{\bar{\rho}\sqrt{T}} \right| \left. \left(\frac{\partial \bar{T}}{\partial \bar{r}} \right) \right|_{\bar{r}=1} \quad (4.21)$$

where

$$\bar{T}_w = \frac{T_w}{T_{O^\infty}}$$

For an adiabatic wall case,

$$\left. \left(\frac{\partial \bar{T}}{\partial \bar{r}} \right) \right|_{\bar{r}=1} = 0 \quad (4.22)$$

At $\bar{r} = 1$ and for noslip case

$$\bar{v} = \bar{u} = 0 \text{ and } \bar{T} = T_w \text{ or } \left. \frac{\partial \bar{T}}{\partial \bar{r}} \right|_{\bar{r}=1} = 0 \quad (4.23)$$

The \bar{r} -coordinate in the physical plane is normalised to the η -coordinate which is also in the physical plane by the following transformations:

$$\bar{r} = 1 + \eta n_{eo} \quad (4.24)$$

where n_{eo} is the total merged layer thickness and η varies from zero to unity. This gives

$$\frac{\partial}{\partial \bar{r}} = \frac{\partial}{\partial \eta} \cdot \frac{\partial \eta}{\partial \bar{r}} = \frac{1}{n_{eo}} \cdot \frac{\partial}{\partial \eta} \quad (4.25)$$

Method of solution

The flow and thermodynamic variables are expanded around the axis of symmetry as follows:

$$\bar{u}(\eta, \theta) = \bar{u}_o(\eta) \sin \theta \quad (4.26a)$$

$$\bar{v}(\eta, \theta) = \bar{v}_o(\eta) \cos \theta \quad (4.26b)$$

$$\bar{p}(\eta, \theta) = \bar{p}_o(\eta) \quad (4.26c)$$

$$\bar{T}(\eta, \theta) = \bar{T}_o(\eta) \quad (4.26d)$$

$$\bar{p}(\eta, \theta) \approx \bar{p}_o(\eta) + \bar{p}_2 \sin^2 \theta \quad (4.26e)$$

$$\bar{\mu}(\eta, \theta) = \bar{\mu}_o(\eta) \quad (4.26f)$$

The form of various expansions is suggested by the boundary conditions at the outer edge of the merged layer, symmetry of the flow around the stagnation line and the fact that pressure inside the merged layer varies as $(\sin^2 \theta)$. The latter statement is conjectured from the following considerations

- (i) Newtonian formula suggests that pressure on the surface of a blunt body varies as $\sin^2 \theta$. Also (ii) pressure behind the shock when it is formed varies as $\sin^2 \theta$. This condition necessitates including the higher order term $\bar{p}_2(\eta) \sin^2 \theta$ as part of the leading term approximations. For this reason, leading term form an indented series. Such considerations are

not available to find correct expansion for density. Within Newtonian approximation, density is infinite in the thin layer near the body while Rankine-Hugoniot relation gives finite value of density behind the shock when the Mach number is large. These considerations do not lead us to suggest a correct expansion for density variation. As such, in the present analysis, density variation near the surface bears some error.

The coefficients in the series expansions and their derivatives are assumed to be of the order of unity. These expansions (4.26a) and (4.26f) are substituted in governing equations (4.11) to (4.16). Collecting like powers of θ the following set of differential equations are obtained:

$$\frac{1 + n_{eo}}{n_{eo}} (\bar{\rho}_o \bar{v}_o) + 2\bar{\rho}_o (\bar{u}_o + \bar{v}_o) = 0 \quad (4.27)$$

$$\frac{\bar{v}_o''}{n_{eo}^2} = \frac{3}{4} \frac{Re_o}{\bar{\mu}_o} \left(\frac{\bar{p}_o'}{n_{eo}} + \frac{\bar{\rho}_o \bar{v}_o \bar{v}_o'}{n_{eo}} \right) - \left(\frac{2}{1+n_{eo}^2} + \frac{\bar{\mu}_o'}{n_{eo} \bar{\mu}_o} \right) \frac{\bar{v}_o'}{n_{eo}} \quad (4.28)$$

$$- \frac{\bar{u}_o'}{2n_{eo}(1+n_{eo}^2)} + \left(\frac{\bar{\mu}_o'}{n_{eo} \bar{\mu}_o} + \frac{7}{2(1+n_{eo}^2)} \right) \frac{\bar{u}_o + \bar{v}_o}{(1+n_{eo}^2)} \quad (4.28)$$

$$\begin{aligned}
 \frac{\bar{u}_o''}{n_{eo}^2} &= \frac{R_{eo}}{\bar{\mu}_o} \left[\frac{2\bar{p}_2}{1+n_{eo}\eta} + \bar{\rho}_o \left(\frac{\bar{v}_o \bar{u}_o'}{n_{eo}} + \frac{\bar{u}_o (\bar{u}_o + \bar{v}_o)}{1+n_{eo}\eta} \right) \right] \\
 &- \frac{\bar{u}_o'}{n_{eo}} \left(\frac{2}{1+n_{eo}\eta} + \frac{\bar{\mu}_o'}{\bar{\mu}_o n_{eo}} \right) + \frac{1}{3} \frac{\bar{v}_o'}{n_{eo} (1+n_{eo}\eta)} \\
 &+ \frac{\bar{u}_o + \bar{v}_o}{1+n_{eo}\eta} \left(\frac{8}{3(1+n_{eo}\eta)} + \frac{\bar{\mu}_o'}{\bar{\mu}_o n_{eo}} \right) \quad (4.29)
 \end{aligned}$$

$$\begin{aligned}
 \frac{\Lambda}{n_{eo}} (1+n_{eo}\eta)^2 \bar{\rho}_o \bar{v}_o \bar{T}_o' &= \frac{(1+n_{eo}\eta)^2}{n_{eo}} \bar{v}_o \bar{\rho}_o' \\
 &+ \frac{1}{Re_o} \frac{1+n_{eo}\eta}{Pr} \left\{ \Lambda \left(2 \frac{\bar{\mu}_o \bar{T}_o'}{n_{eo}} + \frac{(1+n_{eo}\eta)}{n_{eo}^2} (\bar{\mu}_o' \bar{T}_o' + \bar{\mu}_o \bar{T}_o'') \right) \right\} \\
 &+ \frac{2(1+n_{eo}\eta)^2}{n_{eo}^2} \frac{1}{Re_o} \bar{\mu}_o \bar{v}_o^2 + \frac{4}{Re_o} \bar{\mu}_o (\bar{u}_o + \bar{v}_o)^2 \\
 &- \frac{2}{3} \frac{1}{Re_o} \bar{\mu}_o \left(\frac{1+n_{eo}\eta}{n_{eo}} \bar{v}_o' + 2\bar{u}_o + 2\bar{v}_o \right)^2 \quad (4.30)
 \end{aligned}$$

$$\begin{aligned}
 \bar{p}_o &= \frac{\gamma-1}{\gamma} \Lambda \bar{\rho}_o \bar{T}_o \\
 \frac{\bar{p}_2'}{n_{eo}} &= -\frac{1}{2} \frac{\bar{p}_o'}{n_{eo}} + \frac{\bar{\rho}_o \bar{u}_o}{(1+n_{eo}\eta)} (\bar{u}_o + \bar{v}_o) + \frac{1}{2} \frac{\bar{\rho}_o \bar{v}_o \bar{v}_o'}{n_{eo}} \quad (4.31)
 \end{aligned}$$

$$\text{Also, } \mu_o = \sqrt{\bar{T}_o} \quad (4.32)$$

In the above equations, a prime over a variable denote the derivative of the variable with respect to η . These equations are strictly valid at the stagnation line only.

The boundary conditions become,

at the outer edge of the merged layer, $\eta = 1$,

$$\bar{u}_o = 1; \bar{v}_o = -1; \bar{p}_o = 1; \bar{T}_o = 1 - \frac{1}{2\Lambda}; \bar{p}_2 = 0 \quad (4.33)$$

at the surface, $\eta = 0$

$$\bar{u}_o = \sqrt{\frac{\pi\gamma}{2}} \cdot \frac{2-\sigma}{\sigma} \cdot \frac{M_\infty}{Re_o} \sqrt{\frac{T_\infty}{T_{o\infty}}} \cdot \frac{1}{n_{eo}} \cdot \left(\frac{\bar{\mu}_o}{\bar{p}_o \bar{T}_o} \right)^{1/2} \cdot \frac{du_o}{d\eta} \Big|_{\eta=0} \quad (4.34)$$

$$\bar{v}_o = 0 \quad (4.35)$$

$$\bar{T}_o = \bar{T}_w + \left(\frac{\pi\gamma}{2} \right)^{1/2} \left(\frac{2-\sigma}{\sigma} \right) \frac{2\gamma}{\gamma+1} \cdot \frac{M_\infty}{Pr Re_o} \left(\frac{T_\infty}{T_{o\infty}} \right)^{1/2} \frac{1}{n_{eo}} \cdot$$

$$\cdot \left(\frac{\bar{\mu}_o}{\bar{p}_o \bar{T}_o} \right)^{1/2} \cdot \frac{d\bar{T}_o}{d\eta} \Big|_{\eta=0} \quad (4.36)$$

For an adiabatic wall case

$$\left(\frac{d\bar{T}}{d\eta} \right)_{\eta=0} = 0 \quad (4.37)$$

For noslip condition,

$$\bar{u}_o = \bar{v}_o = 0 \quad (4.38)$$

$$\bar{T}_o = \bar{T}_w \quad \text{or} \quad \frac{d\bar{T}_o}{d\eta} = 0 \quad \text{at } \eta = 0 \quad (4.39)$$

Note that both the \bar{r} -line of the η -line lie in the physical plane and the linear relationship between them is given by equation 4.24. When the grids are adapted, grid points in the physical plane become unevenly spaced. But grid points are uniformly spaced in the computational plane, by construction. Hence, the governing equations are solved in the computational plane.

Let ξ be the computational line. The relationship between \bar{r} and ξ or η and ξ are not known, a priori.

Let,

$$\eta \rightarrow \xi(\eta) \quad (4.40)$$

$$\frac{d}{d\eta} = \frac{d}{d\xi} \cdot \frac{d\xi}{d\eta} = \xi_\eta \frac{d}{d\xi} = \frac{1}{\eta_\xi} \frac{d}{d\xi} \quad (4.41)$$

$$\begin{aligned} \frac{d^2}{d\eta^2} &= \frac{d}{d\eta} \left(\frac{d}{d\eta} \right) = \frac{1}{\eta_\xi} \frac{d}{d\xi} \left(\frac{1}{\eta_\xi} \frac{d}{d\xi} \right) \\ &= \frac{1}{\eta_\xi^2} \frac{d^2}{d\xi^2} - \frac{\eta_{\xi\xi}}{\eta_\xi^3} \frac{d}{d\xi} \end{aligned} \quad (4.42)$$

Substituting equations (4.41) and (4.42) in equations (4.27) to (4.32), the following equations in the computational plane are obtained:

$$\frac{1 + \eta n_{eo}}{n_{eo}} - \frac{1}{\eta_\xi} (\bar{p}_o \bar{v}_o)' + 2 \bar{p}_o (\bar{u}_o + \bar{v}_o) = 0 \quad (4.43)$$

$$\begin{aligned}
 \frac{1}{n_{eo}^2} \left[\frac{\bar{v}_o''}{\eta_\xi^2} - \frac{\eta_{\xi\xi}}{\eta_\xi^3} \bar{v}_o' \right] &= \frac{3}{4} \frac{R_{eo}}{\bar{\mu}_o} \left[\frac{\bar{p}_o'}{\eta_\xi n_{eo}} + \frac{\bar{p}_o \bar{v}_o \bar{v}_o'}{\eta_\xi n_{eo}} \right] \\
 &- \left(\frac{2}{1 + \eta n_{eo}} + \frac{\bar{\mu}_o'}{\eta_\xi n_{eo} \bar{\mu}_o} \right) \frac{\bar{v}_o'}{\eta_\xi n_{eo}} \\
 &- \frac{\bar{u}_o'}{2n_{eo} (1 + \eta n_{eo})} - \frac{1}{\eta_\xi} \\
 &+ \left(\frac{\bar{\mu}_o'}{\eta_\xi n_{eo} \bar{\mu}_o} + \frac{7}{2(1 + \eta n_{eo})} \right) \frac{\bar{u}_o + \bar{v}_o}{1 + \eta n_{eo}} \tag{4.44}
 \end{aligned}$$

$$\begin{aligned}
 \frac{1}{n_{eo}^2} \left[\frac{\bar{u}_o''}{\eta_\xi^2} - \frac{\eta_{\xi\xi}}{\eta_\xi^3} \bar{u}_o' \right] &= \frac{R_{eo}}{\bar{\mu}_o} \left[\frac{2\bar{p}_2}{1 + \eta n_{eo}} + \bar{p}_o \left(\frac{\bar{v}_o \bar{u}_o'}{\eta_\xi n_{eo}} + \frac{\bar{u}_o (\bar{u}_o + \bar{v}_o)}{1 + \eta n_{eo}} \right) \right] \\
 &- \frac{\bar{u}_o'}{\eta_\xi n_{eo}} \left(\frac{2}{1 + \eta n_{eo}} + \frac{\bar{\mu}_o'}{\eta_\xi \bar{\mu}_o n_{eo}} \right) + \frac{1}{3} \frac{\bar{v}_o'}{n_{eo} \eta_\xi (1 + \eta n_{eo})} \\
 &+ \frac{(\bar{u}_o + \bar{v}_o)}{1 + \eta n_{eo}} \left(\frac{8}{3(1 + \eta n_{eo})} + \frac{\bar{\mu}_o}{\eta_\xi \bar{\mu}_o n_{eo}} \right) \tag{4.45}
 \end{aligned}$$

(4.45)

$$\frac{\Lambda}{n_{eo}} (1 + \eta n_{eo})^2 \frac{\bar{p}_o \bar{v}_o \bar{T}_o'}{\eta \xi} = \frac{(1 + \eta n_{eo})^2}{n_{eo}} \frac{\bar{v}_o \bar{p}_o'}{\eta \xi}$$

$$\begin{aligned}
 & + \frac{1}{Re_o} \frac{1 + \eta n_{eo}}{Pr} \{ \Lambda \left(\frac{2 \bar{\mu}_o \bar{T}_o'}{\eta \xi n_{eo}} + \frac{1 + \eta n_{eo}}{n_{eo}^2} \left(\frac{\bar{\mu}_o \bar{T}_o'}{\eta \xi} \right)^2 + \bar{\mu}_o \left(\frac{\bar{T}_o'}{2} - \frac{\eta \xi \bar{T}_o'}{\eta \xi^3} \right) \right) \} \\
 & + \frac{2(1 + \eta n_{eo})^2}{n_{eo}^2} \frac{1}{Re_o} \frac{\bar{\mu}_o \bar{v}_o'^2}{\eta \xi^2} + \frac{4}{Re_o} \bar{\mu}_o (\bar{u}_o + \bar{v}_o)^2 \\
 & - \frac{2}{3} \frac{1}{Re_o} \bar{\mu}_o \left(\frac{1 + \eta n_{eo}}{n_{eo}} \frac{\bar{v}_o'}{\eta \xi} + 2\bar{u}_o + 2\bar{v}_o \right)^2
 \end{aligned} \tag{4.46}$$

$$\bar{p}_o = \frac{\gamma-1}{\gamma} \Lambda \bar{p}_o \bar{T}_o \tag{4.47}$$

$$\frac{\bar{p}_2'}{\eta \xi n_{eo}} = - \frac{1}{2} \frac{\bar{p}_o'}{\eta \xi n_{eo}} + \frac{\bar{p}_o \bar{u}_o}{(1 + \eta n_{eo})} (\bar{u}_o + \bar{v}_o) + \frac{1}{2} \frac{\bar{p}_o \bar{v}_o \bar{v}_o'}{\eta \xi n_{eo}} \tag{4.48}$$

$$\bar{\mu}_o = \sqrt{\bar{T}_o} \tag{4.49}$$

Note that in the equations (4.43) to (4.49) dashes denote derivatives with respect to ξ and all the variables, \bar{u}_o , \bar{v}_o , \bar{p}_o , \bar{T}_o , \bar{p}_o , \bar{p}_2 , $\bar{\mu}_o$ and η are now functions of ξ . The computational coordinate ξ is also varied from zero to unity.

Boundary conditions:At $\xi = 1$,

$$\bar{u}_o = 1; \bar{v}_o = -1; \bar{p}_o = 1; \bar{T}_o = 1 - \frac{1}{2\Lambda}; \bar{p}_2 = 0$$

(4.50)

At $\xi = 0$,

$$\bar{u}_o = \sqrt{\frac{\pi\gamma}{2}} \frac{2-\sigma}{\sigma} \frac{M_\infty}{Re_o} \sqrt{\frac{T_\infty}{T_{o\infty}}} \frac{1}{n_{eo}} \left(\frac{\bar{\mu}_o}{\bar{\rho}_o \bar{T}_o^{1/2}} \frac{1}{\eta_\xi} \frac{d\bar{u}_o}{d\xi} \right)_{\xi=0}$$

(4.51)

$$\bar{v}_o = 0$$

(4.52)

$$\bar{T}_o = \bar{T}_w + \left(\frac{\pi\gamma}{2} \right)^{1/2} \left(\frac{2-\alpha}{\alpha} \right) \frac{2\gamma}{\gamma+1} \frac{M_\infty}{Pr Re_o} \left(\frac{T_\infty}{T_{o\infty}} \right)^{1/2}.$$

$$\frac{1}{n_{eo}} \left(\frac{\bar{\mu}_o}{\bar{\rho}_o \bar{T}_o^{1/2}} \frac{1}{\eta_\xi} \frac{d\bar{T}_o}{d\xi} \right)_{\xi=0}$$

(4.53)

For adiabatic wall case

$$\frac{d\bar{T}_o}{d\xi} \Big|_{\xi=0} = 0$$

(4.54)

For noslip case, at $\xi = 0$

$$\bar{u}_o = \bar{v}_o = 0$$

(4.55)

$$\bar{T}_o = \bar{T}_w \quad \text{or} \quad \frac{d\bar{T}_o}{d\xi} = 0$$

(4.56)

4.3 Numerical Method

The governing equations consist of three second order differential equations namely equations (4.44), (4.45) and (4.46) for the variables \bar{v}_o , \bar{u}_o and \bar{T}_o respectively. These equations may be written in the form

$$v_o (\bar{v}_o'', \bar{v}_o', \bar{u}_o', \bar{u}_o'', \dots) = 0 \quad (4.57)$$

$$u_o (\bar{u}_o'', \bar{u}_o', \bar{u}_o', \bar{v}_o'', \dots) = 0 \quad (4.58)$$

$$t_o (\bar{T}_o'', \bar{T}_o', \bar{u}_o', \bar{u}_o'', \bar{v}_o', \bar{v}_o'', \dots) = 0 \quad (4.59)$$

and the rest are first order equations.

It is desired to obtain the solution in the range $[0, 1]$ in the computational domains, ξ , which is divided into equal parts, each of length, $\Delta = \frac{1}{NDIV}$. Thus, the total number of grid points is $NDIV+1$. In equations (4.57) to (4.59), the first and second order derivatives are replaced by

$$x_N' = \frac{x_{N+1} - x_{N-1}}{2 \Delta} \quad (4.60)$$

$$x_N'' = \frac{x_{N+1} - 2x_N + x_{N-1}}{2 \Delta^2} \quad (4.61)$$

where x_N represents the value of any one of the variables

\bar{u}_o , \bar{v}_o , \bar{T}_o , \bar{p}_o , \bar{p}_2 , $\bar{\rho}_o$ or η at the N^{th} mesh point.

Here, $N = 1$ represents the surface and $N = NDIV + 1$ represents the free stream location. That is, $N = 1$ corresponds to

$\xi = 0$ and $N = NDIV + 1$ corresponds to $\xi = 1$. The difference equations so obtained for each grid point are solved by SAR method. The first order equations (4.43) and (4.48) are solved by trapezoidal, Simpson and Weddle's rules as in section 4.4.

Method of Successive Accelerated Replacement:

Equations (4.57) to (4.59) form three sets of algebraic equations each set containing $(NDIV - 1)$ number of equations (N varies from 2 to $NDIV$). The boundary conditions for these three variables for $N = 1$ and $N = NDIV + 1$ are as follows :

For the slip case

$$\bar{u}_{o_1} = \left(\frac{\pi\gamma}{2}\right)^{1/2} \frac{2-\sigma}{\sigma} \frac{M_\infty}{Re_o} \left(\frac{T_\infty}{T_{o^\infty}}\right)^{1/2} \frac{1}{n_{eo}} \left(\frac{\bar{\mu}_{o_1}}{\bar{\rho}_{o_1} \bar{T}_{o_1}}\right)^{1/2} \left[\frac{1}{n_{eo}} \right. \\ \left. \frac{4\bar{u}_{o_2} - \bar{u}_{o_3} - 3\bar{u}_{o_1}}{2\Delta} \right] - u_{o_1} \quad (4.62)$$

$$\bar{v}_{o_1} = 0 \quad (4.63)$$

$$\bar{T}_{o_1} = \bar{T}_w + \left(\frac{\pi\gamma}{2}\right)^{1/2} \frac{2-\alpha}{\alpha} \frac{2\gamma}{\gamma+1} \frac{M_\infty}{Pr Re_o} \left(\frac{T_\infty}{T_{o^\infty}}\right)^{1/2} \\ \cdot \frac{1}{n_{eo}} \left(\frac{\bar{\mu}_{o_1}}{\bar{\rho}_{o_1} \bar{T}_{o_1}^{1/2}}\right) \left[\frac{4T_{o_2} - T_{o_3} - 3T_{o_1}}{2\Delta} \right] \quad (4.64)$$

$$\bar{u}_{o_{NDIV+1}} = 1; \bar{v}_{o_{NDIV+1}} = -1; \bar{T}_{o_{NDIV+1}} = 1 - \frac{1}{2\Lambda} \quad (4.65)$$

For noslip case,

$$\bar{u}_{o_1} = \bar{v}_{o_1} = 0, \bar{T}_{o_1} = \bar{T}_w \quad (4.66)$$

$$\bar{u}_{o_{NDIV+1}} = 1, \bar{v}_{o_{NDIV+1}} = -1, \bar{T}_{o_{NDIV+1}} = 1 - \frac{1}{2\Lambda} \quad (4.67)$$

Each set of $(NDIV-1)$ number of equations is solved by the method of Successive Accelerated Replacement (SAR).

This method was originally developed by Lieberstein³² for the iterative solution of nonlinear algebraic equations.

SAR method is a generalization of Young's³³ method of successive overrelaxation of the iterative solution of linear algebraic equations. Lew³⁴ first applied this method to solve the Blasius equation and obtained 1.7 as the optimum value of the acceleration parameter. Later, Dellinger³⁵ applied this method to non-equilibrium viscous layer stagnation point flows. Jain and Adimurthy²⁰ applied this method to hypersonic merged layer flow in the stagnation region and found that this method gave reasonably accurate results.

In this method, corrections applied to the values of the variables at each mesh point are controlled by the acceleration factors which prevent the iterative scheme from diverging. This scheme is successive replacement in the sense that new variables are made use of as soon as they are available.

This method decouples the system of algebraic equations. In each iteration, it involves the use of one particular equation only for the correction of one unknown variable in that equation. Also in each iteration the boundary conditions are always satisfied. This method is economic in computer time as well. Due to all these points the method of Successive Accelerated Replacement is applied to the system of equations (4.57) to (4.59).

Now, the correction procedure for one of the variables, say \bar{v}_o is described here. The other two variables \bar{u}_o and \bar{T}_o governed by the second order equations will be corrected in the same way. The $(k+1)^{th}$ approximation to \bar{v}_o at the N^{th} mesh point is calculated from

$$\bar{v}_o^{k+1} = \bar{v}_o^k - w_{v_o} \frac{\frac{v_o^N}{d\bar{v}_o^N}}{\frac{d\bar{v}_o^N}{d\bar{v}_o^N}} \quad (4.68)$$

The number w_{v_o} is called the acceleration factor.

It is calculated as follows:

First it is required that

$$\frac{\frac{v_o^{k+1} - v_o^k}{\bar{v}_o^N}}{\frac{v_o^k - v_o^{k-1}}{\bar{v}_o^N}} = w_{v_o} \left| \frac{\frac{v_o^N}{d\bar{v}_o^N}}{\frac{v_o^k}{\bar{v}_o^N} \frac{d\bar{v}_o^N}{d\bar{v}_o^N}} \right| < \epsilon \quad (4.69)$$

where ϵ is a prescribed small parameter.

Let,

$$\sigma_{v_o} = \bar{v}_{o_N}^k \epsilon \frac{dv_{o_N}}{d\bar{v}_{o_N}} \cdot \frac{1}{v_{o_N}} \quad (4.70)$$

If $\sigma_{v_o} < 1$ then w_{v_o} is taken to be σ_{v_o} and if $\sigma_{v_o} \geq 1$ then w_{v_o} is taken to be unity.

This procedure ensures that the correction applied at each iteration is never greater than ϵ times the value of the variable at that point in the previous iteration. The correction starts from the point $N = 2$ and continues upto $N = NDIV$.

4.4 Solution Procedure

To start with, an initial profile for the flow variables satisfying the boundary conditions is chosen. The value of n_{eo} is prescribed initially and then corrected in successive iteration. Following equation (4.69), the corrections are first made to the variables \bar{v}_o , \bar{u}_o and \bar{T}_o in equations (4.57) to (4.59), in that order, for grid points $N = 2$ to $N = NDIV$. Then \bar{p}_o and $\bar{\mu}_o$ are calculated from the equation of state, equation (4.47) and the viscosity-temperature relation, equation (4.49) respectively. $\bar{\rho}_o$ and \bar{p}_2 are obtained from the continuity equation, equation (4.43) and the equation (4.48) respectively. Since

the values of $\bar{\rho}_o$ and \bar{p}_2 are known at the free stream end ($\bar{\rho}_o^{NDIV+1} = 1.0$ and $\bar{p}_2^{NDIV+1} = 0.0$) but unknown at the body surface, the integration starts from the free stream.

Now, the procedure for calculating $\bar{\rho}_o$ and \bar{p}_2 will be described. At the last but one point from the free stream, the values of $\bar{\rho}_o$ and \bar{p}_2 are found by Trapezoidal rule. The values at the next four points are calculated by using the Simpson's $3/8^{th}$ rule. At the remaining points except the point on the boundary surface, Weddle's rule is used to evaluate \bar{p}_2 and $\bar{\rho}_o$.

$$\int \frac{\bar{\rho}_o}{\bar{\rho}_o} d\xi = \int \frac{\eta \xi^n n_{eo}}{(1+n_{eo}n)\bar{v}_o} [-2\bar{u}_o - 2\bar{v}_o - \frac{1+n n_{eo}}{\eta \xi^n n_{eo}} \bar{v}'] d\xi \quad (4.71)$$

$$\int \bar{p}_2' d\xi = \eta \xi^n n_{eo} \int \left[\frac{\bar{\rho}_o \bar{u}_o}{(1+n n_{eo})} - \frac{\bar{\rho}_o'}{2\eta \xi^n n_{eo}} + \frac{\bar{\rho}_o \bar{v}_o \bar{v}_o'}{2\eta \xi^n n_{eo}} \right] d\xi \quad (4.72)$$

Weddle's rule is used to find the value of \bar{p}_2 at the surface also.

Due to a singularity in equation (4.71) at the surface ($\therefore \bar{v}_{o1} = 0$), the density at the surface has a finite value only if

$$\bar{v}_o' = -2\eta \xi_1^n n_{eo} \bar{u}_{o1}' \text{ for slip case} \quad (4.73)$$

$$= 0 \text{ for no-slip case.}$$

This condition is used to improve the value of \bar{v}_o at the second grid point.

If equation (4.71) is to be used to evaluate the density at the surface, L'Hospital's rule is to be applied twice. However this approach is not adopted here. In general, the density at the surface is very high, particularly for the cold wall case. It has a very large gradient at the body surface. So density at the surface is calculated from the equation of state i.e. equation (4.47) while the pressure at the surface is calculated from the expression.

$$\bar{p}_{o_1} = \bar{p}_{o_2} - \bar{p}'_{o_1} \cdot \Delta \quad (4.74)$$

where \bar{p}'_{o_1} is calculated from equation (4.48) by evaluating it at the surface. This gives.

$$\begin{aligned} \bar{p}'_{o_1} &= \frac{4 \eta \xi_1 \bar{\mu}_{o_1}}{3 Re_o n_{eo}} \left\{ \left[\frac{\bar{v}''_{o_1}}{\eta \xi_1^2} - \frac{\eta \xi_1 \bar{v}'_{o_1}}{\eta \xi_1^3} \right] + \right. \\ &+ \left(2 + \frac{\bar{\mu}'_{o_1}}{\eta \xi_1 n_{eo} \bar{\mu}_{o_1}} \right) \frac{\bar{v}'_{o_1} n_{eo}}{\eta \xi_1} + \frac{\bar{u}'_{o_1} n_{eo}}{2 \eta \xi_1} - \\ &- \left. \left(\frac{7}{2} + \frac{\bar{\mu}'_{o_1}}{\eta \xi_1 n_{eo} \bar{\mu}_{o_1}} \right) (\bar{u}_{o_1} + \bar{v}_{o_1}) n_{eo}^2 \right\} - \bar{\rho}_{o_1} \bar{v}_{o_1} \bar{v}'_{o_1} \quad (4.75) \end{aligned}$$

This process of iteration continues till proper convergence of the variables is achieved. The value of n_{eo} is corrected in each iteration till the temperature profile reaches the outer boundary conditions asymptotically. It is found that at this stage, other variables of the flow also approach the freestream values asymptotically.

4.5 Grid Adaptation

In the merged layer flow gradients of the flow variables are large near the surface and in the shock wave like outer region of the flow field whose location is not known a priori. Moreover the shock wave like region develops as the integration proceeds. Under such flow conditions the adaptive grid technique has to be employed so that more grid points move automatically to the region of high gradients of the flow field. In the present investigation the following weight function is used

$$w(\xi_i) = 1 + A \left| \frac{df}{d\xi} \right|_i + B \left| \frac{d^2f}{d\xi^2} \right|_i \quad \text{for } 1 \leq i \leq \text{NDIV}+1$$

(4.76)

which is averaged as

$$w(\xi_i) = \frac{w(\xi_i) + w(\xi_{i+1})}{2}, \quad \text{for } 1 \leq i \leq \text{NDIV}$$

Here, f is any dependent variable and A and B are constants which indicate the relative importance of the gradients and the curvature of the profile of the variable f . Following Nakahashi and Deiwert¹⁴, the grid size in the physical plane is

related to the weight function in the computational plane in the following manner:

$$\Delta \bar{r}_i = \frac{n_{eo}}{w(\xi_i) \sum_{i=1}^{NDIV} \frac{1}{w(\xi_i)}} \quad (4.77)$$

where $n_{eo} = \sum \Delta \bar{r}_i$.

It could be seen from equation (4.77) that as the weight function increases in magnitude, the grid size decreases and vice versa.

Proper choice of the variable f in equation (4.76) is made by considering the conditions at 92 Km. altitude of the shuttle flight conditions using the data from Table (4.1). Here, Re_o is calculated from Sutherland viscosity law. This choice of f is not altered for other altitudes. Figure (4.2) could be referred to understand the following discussion more easily.

4.5.1 Choice of the Constants A and B

There is no fixed criteria as how to choose the constants A and B. The best and obvious method, for the present, is trial and error. The dependent variable in the weight function is chosen either as temperature alone or the normal component of velocity alone or a combination of both in the manner stated in the next section. For each of these choices the value of A is varied from 0.2 to 1.6 in steps of 0.2. For each value of A, the following set of values of B are tried : 0.0, 0.15, 0.20, 0.4 and 0.6.

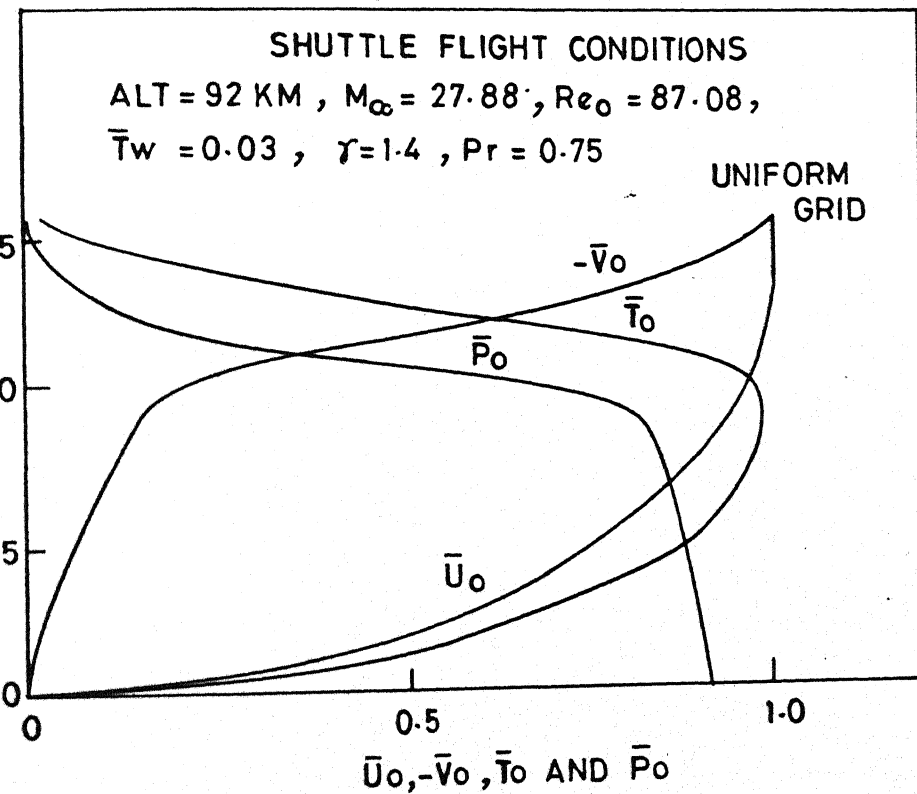


FIG. 4.2 PROFILES OF $\bar{U}_0, -\bar{V}_0, \bar{T}_0$ AND \bar{P}_0 WITH UNIFORM GRIDS

The best choice of A and B is the one which leads to faster convergence, resolves the flow field adequately and gives accurate values of C_H at the surface. For the prescribed conditions at 92 Km, it was found that the values $A = 1$ and $B = 0.15$ satisfied best the above criterion.

The gradients and curvatures in the shock wave like region increase as the Reynolds number increases. A single set of values of A and B is not adequate to resolve the flow in the entire range of the Reynolds number. It was found that $A = 1$ and $0.0 \leq B \leq 0.4$ gives satisfactory results for the entire range of Reynolds number tested.

It was further found that the constants A and B also depend upon the number of grid points chosen. This point is illustrated at appropriate places in the section entitled "Discussion of Results".

4.5.2 Choice of the Dependent Variable in the Weight Function w

At low Reynolds number, the shock is diffused and the gradients are large near the surface than in the shock wave like outer region (See Fig. 4.3). At higher values of Reynolds number, a distinct shock is found and the gradients of the flow variables \bar{T}_o and \bar{v}_o are large in the shock wave like region in comparison to the gradients in the inner viscous region near the surface. In the shock wave like region, the curvature of the profiles of the normal component of velocity is greater than the curvature of the profile of the temperature (See Figs. 4.2 and 4.7). Thus, it was found that when temperature alone

was taken as the dependent variable in the weight function, much finer grids were obtained near the surface and coarser grids in the outer shock wave like region. When the normal component of velocity only was used as the dependent variable in the weight function, finer grids were obtained in the outer shock wave like region and coarse grids were obtained in the viscous region near the surface. At this stage further trials were made with the profiles of tangential component of velocity \bar{u}_o , density $\bar{\rho}_o$, pressure \bar{p}_o and mass flux $\bar{\rho}_o \bar{v}_o$ as the dependent variable in the weight function, under the prescribed conditions and with the set of constants $A = 1.0$ and $B = 0.2$. It was found that each of them gave unsatisfactory grids. As such, it can safely be concluded from the above that temperature ought to be used as the dependent variable in the weight function to resolve the flow near the surface and the normal component of velocity as the dependent variable to resolve the flow field in the rest of the field. From a comparative study of the gradients and curvatures of the profiles of temperature and normal component of velocity in most of the cases, it was found desirable to define the weight function with reference to the temperature for the first ten grid points and with reference to the normal component of velocity for the rest of the grid points in the flow field.

4.6 Discussion of Results:

Two kinds of study were carried out to determine the effectiveness and usefulness of the adaptive grid technique. The first study was carried out (1) at $M_\infty = 24.95$ and $Re_\infty = 27.74$ with cold wall condition and (2), at $M_\infty = 10.0$ and $Re_\infty = 87.08$ with insulated wall conditions.

For cold wall case, using linear profile for \bar{u}_0 , \bar{T}_0 and \bar{p}_0 and quadratic profile for \bar{v}_0 as the initial profiles, converged solutions are sought, on both uniform and adapted grids, by reducing the number of grid points from 61 to 16. Computations are carried out with the constant B taking the values of 0.0 and 0.15 respectively. When $B = 0$ curvature term in w is not considered and when $B = 0.15$ curvature term is considered. CPU time required and number of iterations taken to arrive at the converged results are given in Table (4.2) along with the corresponding C_H values for 61, 31 and 16 grids.

It could be seen from Table (4.2) that when the number of grid points is 61 or 31, solutions with the adapted grids took considerably more number of iterations and larger CPU-time in comparison to the solution with uniform grids. Both the approaches gave almost the same value of C_H and the maximum temperature (Fig. 4.4). Results with the adapted grids with $B = 0.15$ took larger number of iterations and more CPU-time. It could be seen from Table (4.2) that solutions with uniform grids failed to converge with 16 grid points and solutions with adapted grid

with $B = 0$ gave a value of C_H which is much different from the value of 0.433 obtained with 61 grid points on a uniform grid. But with $B = 0.15$, the resulting value of C_H from solutions on the adapted grid agreed well with the value obtained on a uniform grid with 61 grid points, although compared to the case with $B = 0.0$ and 16 grid points it took more time and iterations. Figure (4.3) shows the profiles on a uniform grid with 61 grid points and an adapted with 16 grid points and with $B = 0.15$. Both the profiles agree well with each other.

Table 4.3 gives the results for the condition of $M_\infty = 10.0$ and $Re_\infty = 87.08$ and using insulated wall boundary condition. Using 61 grid points, it could be seen that the results with adapted grid with $B = 0.0$ in the weight function took lesser number of iterations and lesser CPU-time than the results with uniform grids. These conditions are quite different from the results shown in Table 4.2 for the shuttle flight conditions at 99.49 Km altitude and cold wall conditions. The reason for the anomaly lies in the vastly different nature of the profiles of temperature and normal component of velocity between the two cases. For example ~~to~~ for the insulated wall case, the temperature profile in the viscous region near the wall is almost perpendicular to the wall and varies almost linearly in the outer, thick shock wave like region. Thus the variation

UNIFORM GRID (61 POINTS)

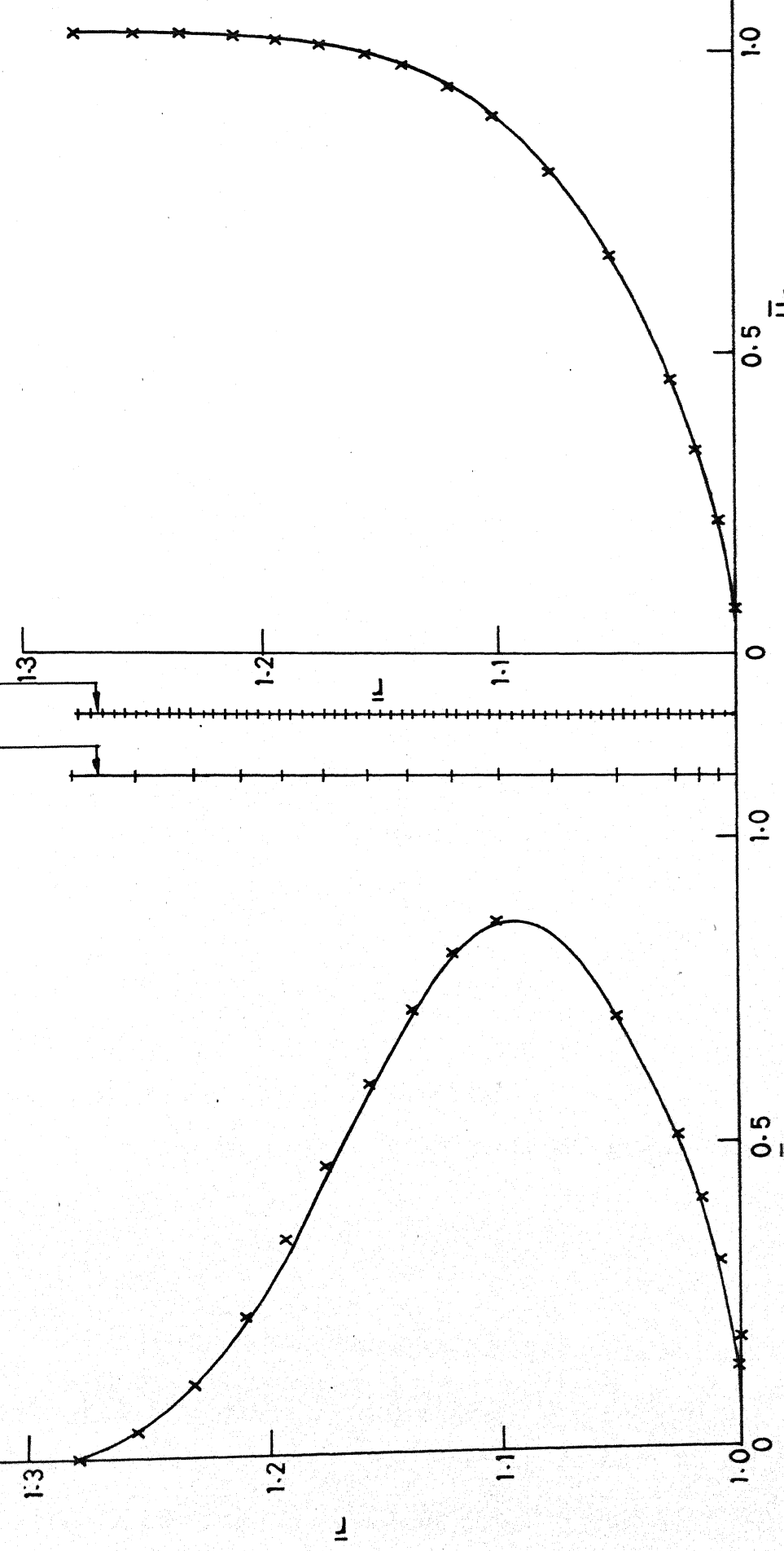
× × × ADAPTED GRID (16 POINTS)
 $A = 1.0, B = 0.15$

SHUTTLE FLIGHT CONDITIONS

ALT. = 99.49 KM, $M_\infty = 27.14$,
 $Re_0 = 24.73, \gamma = 1.4$
 $Pr = 0.75, \bar{T}_w = 0.025$

GRID LOCATION

UNIFORM
ADAPTED



(a) TEMPERATURE PROFILES

(b) TANGENTIAL VELOCITY PROFILES

FIG. 4.3 COMPARISON OF THE FLOW FIELD WITH UNIFORM AND ADAPTED GRIDS

in the adapted grid sizes due to variation in curvature do not play any significant role. Simply gradient variations are enough to give reasonably accurate grid size for faster convergence.

In the second study, computations of the governing equations for the merged layer have been carried out for the shuttle flight condition from 104.93 Km. to 85.74 Km altitude (Table 4.1). Here the Reynolds number was calculated using Sutherland law of viscosity and it varied from 10.28 to 260 while the Mach number varied slightly in the entire trajectory. Here, n_{eo} is not allowed to increase beyond its value at $Re_o = 110$. Variation of the maximum temperature \bar{T}_{max} with uniform and adapted grids against Reynolds number is plotted in Fig. 4.4. Also, the value of post shock temperature obtained from the Rankine-Hugoniot relations is plotted in Fig. 4.4. From Fig. 4.4, it could be seen that the values of \bar{T}_{max} is exactly the same for both uniform and adapted grids upto $Re_o = 160$. Also, upto $Re_o = 160$, the detailed structure of the flow for the two approaches agreed reasonably well (see Fig. 4.3 for $Re_o = 24.73$). For Re_o above 70, a distinct shock and a boundary layer with an inviscid flow in between is formed. As such the predicted \bar{T}_{max} agreed with R.H. Value of 0.972 with reasonable accuracy, maximum error being 1.5 percent. For the range of Reynolds number $160 \leq Re_o \leq 260$, the results with uniform grids did converge by satisfying the convergence criterion but they are in error in that \bar{T}_{max} decreased with increase of Reynolds number which is physically

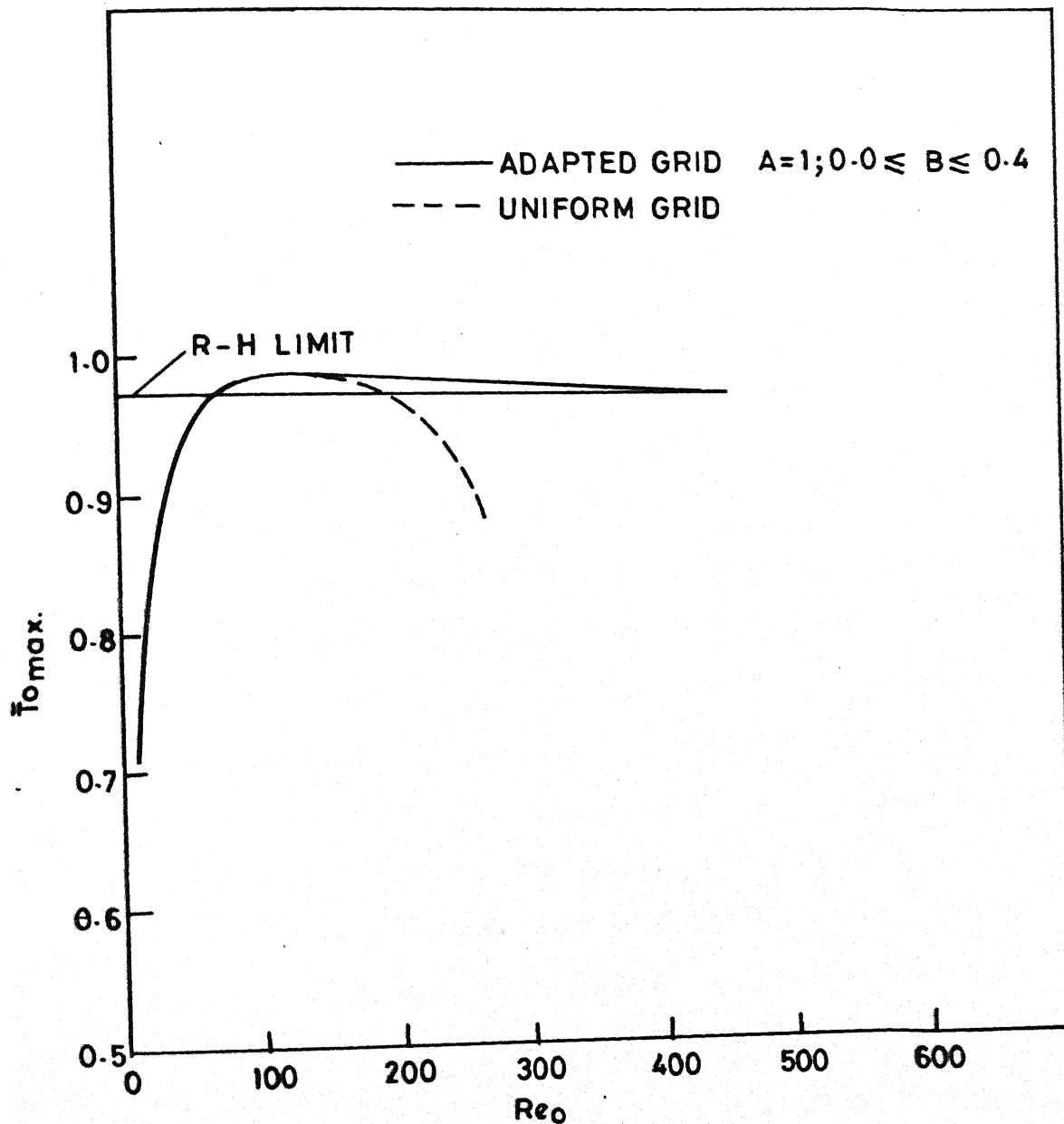


FIG. 4.4 COMPARISON OF T_{max} WITH UNIFORM GRIDS AND ADAPTED GRIDS WITH RANKINE - HUGONIOT POST-SHOCK TEMPERATURE FOR $10.28 \leq Re_0 \leq 430$

unplausible. On the other hand, the results with adapted grids for $160 \leq Re_o \leq 260$ gave the correct variation of \bar{T}_{max} as it agreed with R.H values. Besides, with adapted grids the computation could be extended upto $Re_o = 430$. At this value of Re_o it could be expected reasonably well that the results of the merged layer theory has approached the upper limit of the boundary layer theory. Hence, from the above discussion it could be concluded that in the denser region of the shuttle flight, adapted grid solution gave physically accurate results and extended the range of validity of the merged layer model of the flow field to a reasonably large Reynolds number.

In Fig. 4.5 the converged profiles of \bar{u}_o , $-\bar{v}_o$ and \bar{T}_o on both uniform and adapted grids at $Re_o = 230.08$ are plotted. In Fig. 4.6 the temperature profile alone is plotted for both uniform and adapted grids at $Re_o = 260.08$. It could be seen from Fig. 4.6 with uniform grids, the temperature tends to decrease in the inviscid zone and attains a value of $\bar{T}_{max} = 0.89$ while with adapted grid, the temperature almost remains constant and attains a maximum value of 0.98. Moreover the number of grid points in the shock wave like region on uniform grids is three which is hardly sufficient to resolve such steep gradients as those existing in the shock. But the number of grid points in the shock wave like region on the adapted grids is 9. Considering that the total number of grid points is only 31, the ability of the

SHUTTLE FLIGHT CONDITIONS

$M_\infty = 26.63$, $Re_\infty = 230$, $\bar{T}_w = 0.042$

$\gamma = 1.4$, $Pr = 0.75$

— ADAPTED GRID $A = 1$; $B = 0.15$
 - - - UNIFORM GRID

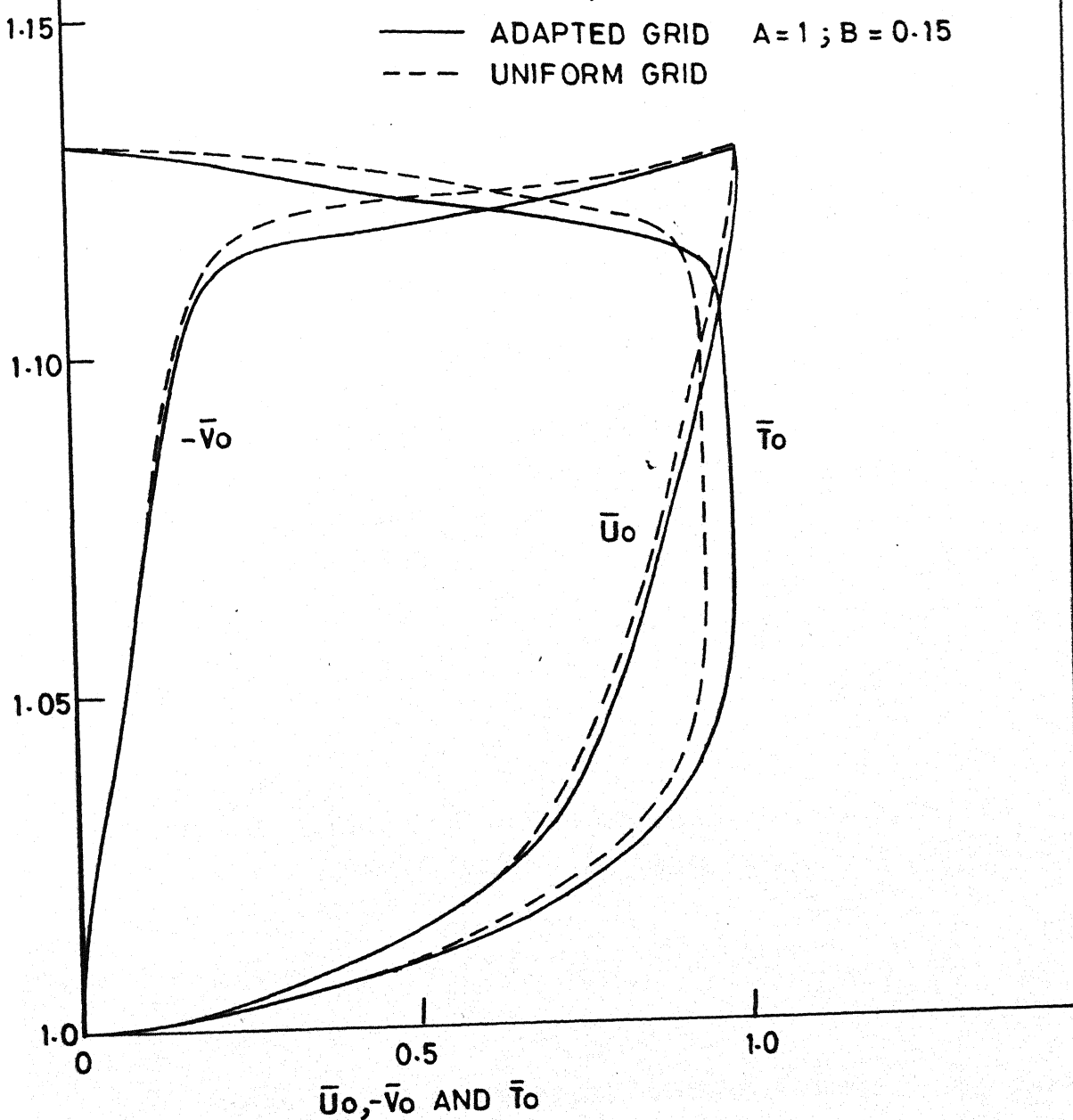


FIG. 4.5 COMPARISON OF \bar{U}_0 , $-\bar{V}_0$ AND \bar{T}_0 AT $Re_\infty = 230$

SHUTTLE FLIGHT CONDITIONS
 $ALT = 85.74$, $M_\infty = 26.63$, $Re_0 = 260$,
 $\bar{T}_w = 0.042$, $\gamma = 1.4$, $Pr = 0.75$
— ADAPTED $A = 1.0$; $B = 0.15$
--- UNIFORM

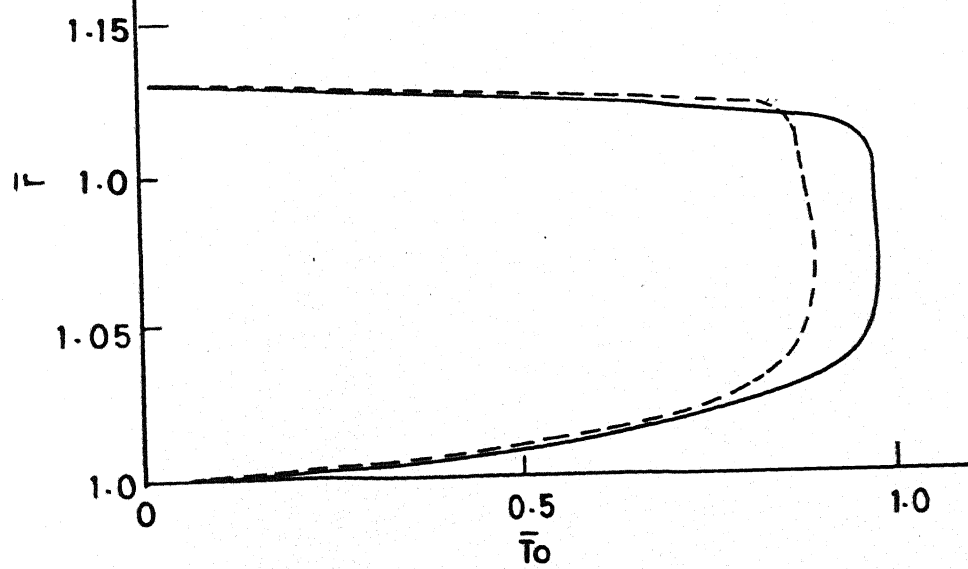


FIG. 4.6 TEMPERATURE PROFILES WITH UNIFORM AND
ADAPTED GRIDS AT $Re_0 = 260$

adapting technique to put 9 grid points in the shock wave like region is highly desirable. In Fig. 4.7, the profiles of \bar{u}_o , $-\bar{v}_o$, \bar{T}_o and \bar{p}_o on an adapted grid are shown at $Re = 400$. These profiles indicate a very thin and strong shock.

In Figs. 4.8 and 4.9, heat transfer coefficient at the surface C_H is plotted against Knudsen's number and Reynold's number respectively.

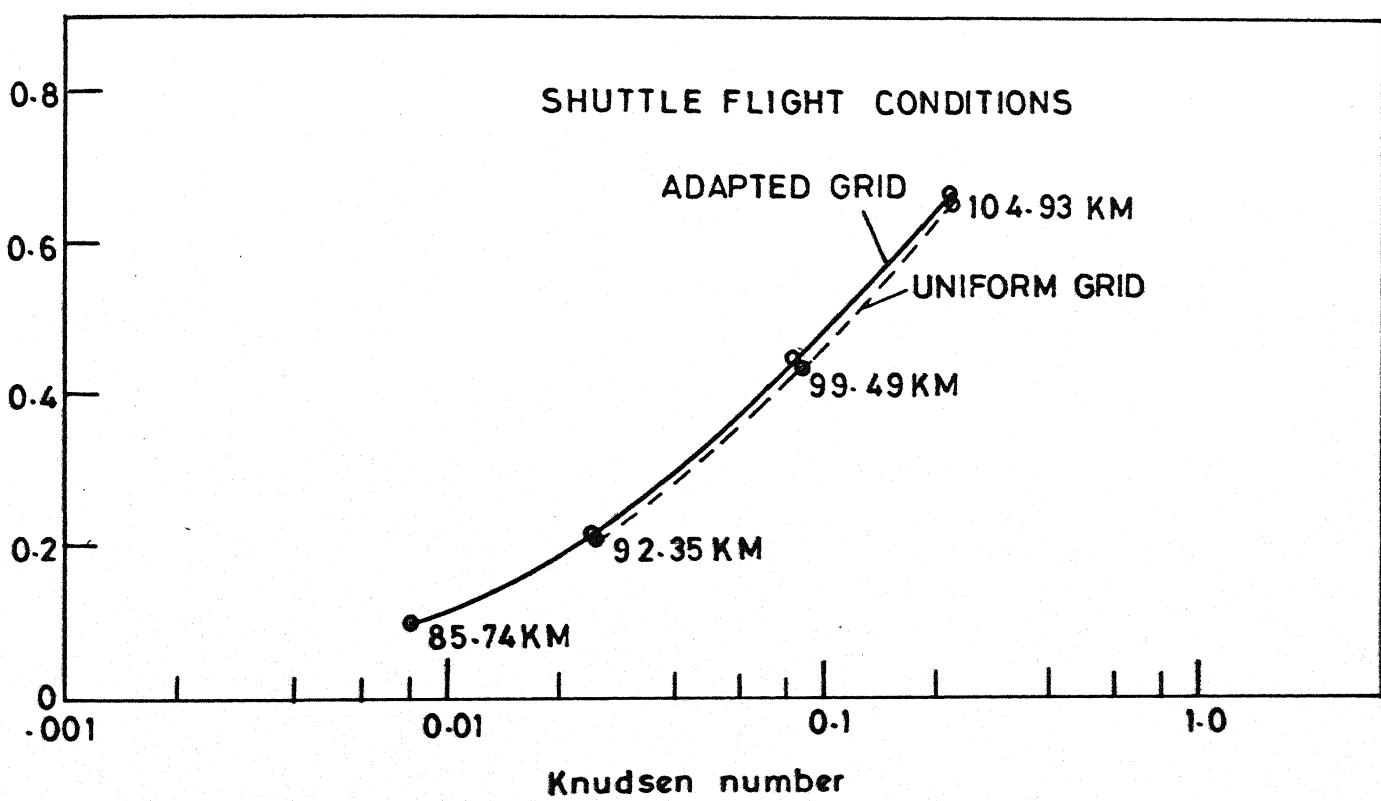


FIG. 4.8 COMPARISON OF HEAT TRANSFER COEFICIENT, C_H , WITH UNIFORM AND ADAPTED GRIDS FROM 104.93 KM TO 85.74 KM ALTITUDE

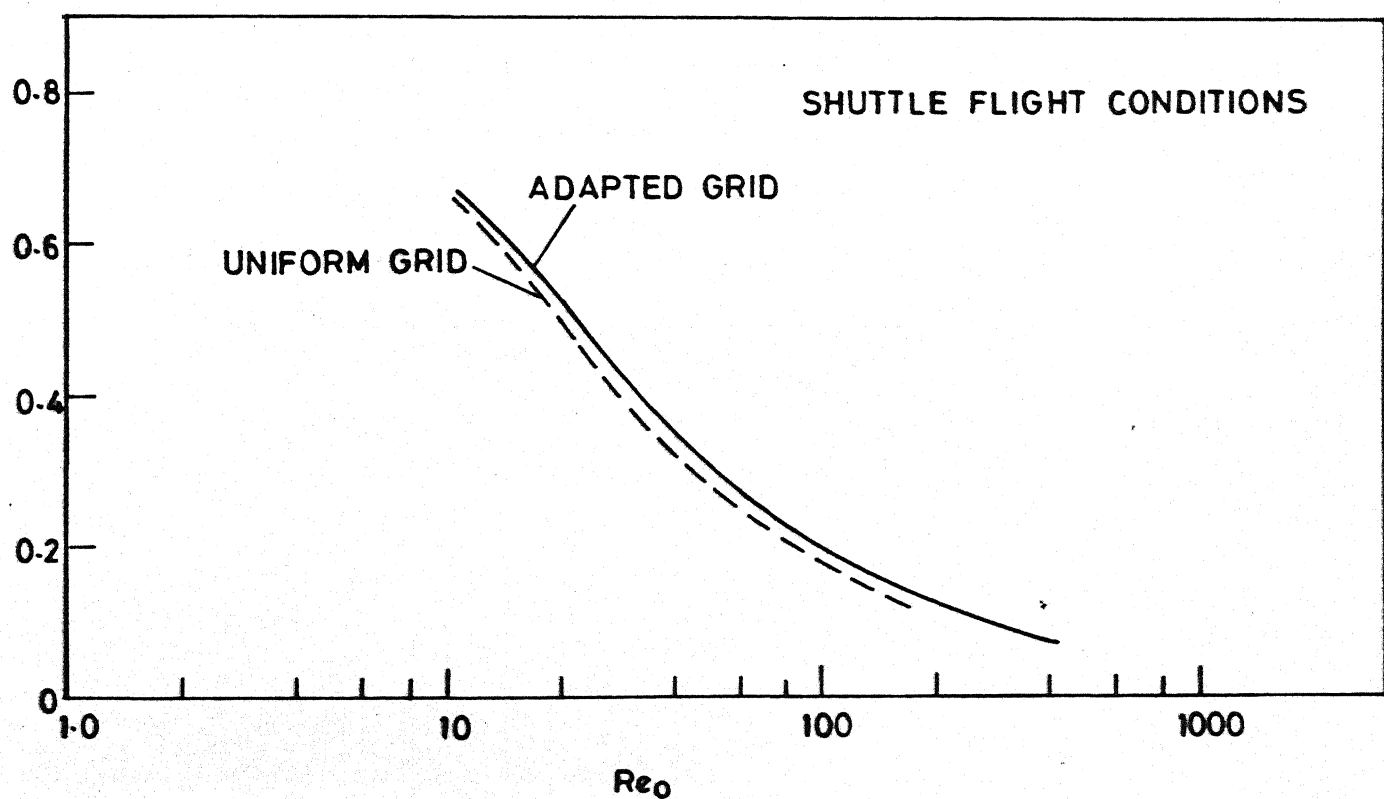


FIG. 4.9 COMPARISON OF HEAT TRANSFER COEFFICIENT, Ch , WITH UNIFORM AND ADAPTED GRIDS FROM 104.93 KM TO 85.74 KM ALTITUDE

Table 4.1 : Input Data Shuttle Flight Conditions

Altitude Km	Body radius cm	T _{wall} °K	ρ _∞ gm/cm ³	T _∞ °K	U _∞ cm/r	Re _∞	M
104.93	136.2	506.5	0.246x10 ⁻⁹	223.0	747000	10.28	24.95
99.49	136.2	705.0	0.591x10 ⁻⁹	190.0	750000	34.74	27.14
92.35	129.6	921.5	0.218x10 ⁻⁸	180.0	750000	87.08	27.88
85.74	132.2	1197.0	0.637x10 ⁻⁸	198.9	753000	258.08	26.63

Table 4.2 : Shuttle Flight Conditions - Cold Wall

Alt = 99.49 Km, $M_{\infty} = 27.14$ $Re_{\infty} = 24.74$, $\gamma = 1.4$, $T_w = 0.025$

Points	Nature of the grid	CPU-time min:sec	ITER	C_H
61	Uniform	1:57.63	1600	0.433
61	Adapted $A = I$; $B = 0$	2:15.18	1800	0.444
61	Adapted $A = I$; $B = 0.15$	3:27.74	2300	0.433
31	Uniform	40.57	1100	0.401
31	Adapted $A=I$; $B = 0$	45.58	1200	0.426
31	Adapted $A=I$; $B = 0.15$	1:47.75	2000	0.414
16	Uniform	did not converge upto 4000 iterations		
16	Adapted $A = 1$; $B=0$	24.24	1200	0.365
16	Adapted $A=1;B=0.15$	22.48	1300	0.428

Table 4.3 : Insulated Wall

$M_\infty = 10.00$; $Re_{\infty} = 87.08$; $\gamma = 1.667$; $Pr = 0.75$; $T_w = 1.0$

Grid points	Nature of the grid	CPU-time min/sec	ITER	C_H
61	Uniform	1:28.84	1400	-0.006
61	Adapted $A=1; B=0$	1:15.57	1200	-0.005
21	Uniform	did not converge upto 4000 iterations		
21	Adapted	20.32	800	+0.002

REFERENCES

1. Winslow, A.M., "Numerical Solution of the Quasilinear Poisson Equation in a Non-Uniform Triangular Mesh", *J. Comp. Phys.*, Vol. 2 (1966), p. 149.
2. Thompson, J.F., Thames, F.C. and Mastin, C.W., "Automatic Numerical Generation of Body-Fitted Curvilinear Coordinate System for Field Containing any Number of Arbitrary Two-dimensional Bodies", *J. of Comp. Phys.*, Vol. 15 (1974), p. 299.
3. Thames, F.C., Thompson, J.F., Mastin, C.W. and Walker, R.W., "Numerical Solution for Viscous and Potential Flows about Arbitrary Two-dimensional Bodies using Body-fitted Coordinate Systems", *J. Comp. Phys.*, Vol. 24 (1977), p. 245.
4. Thompson, J.F., Thames, F.C. and Mastin, C.W., "TOMCAT - A Code for Numerical Generation of Boundary Fitted Curvilinear Coordinate Systems on Fields Containing any Number of Arbitrary Two-dimensional Bodies", *J. Comp. Phys.*, Vol. 24 (1977), p. 274.
5. Thompson, J.F., Warsi, Z.U.A., Mastin, C.W., "Numerical Grid Generation - Foundation and Applications", North Holland, NY (1986).
6. Coleman, R.M. and Haussling, H.J., "A Method for Generation of Orthogonal and Nearly Orthogonal Boundary Fitted Coordinate Systems", *J. Comp. Phys.*, Vol. 43 (1981), pp. 373-381.
7. Brackbill, J.U. and Saltzman, J., "Adaptive Zoning for Singular Problems in Two Dimensions", *J. Comp. Phys.*, Vol. 46 (1982), pp. 342-368.
8. White, Jr., A.B., "On the Numerical Solution of Initial/Boundary - Value Problem in One Space Dimensions", *SIAM J. Numer. Anal.*, Vol. 19 (1982), p. 683.
9. Dwyer, H.A., Kee, R. and Sanders, B., "Adaptive Grid Method for Problems in Fluid Mechanics and Heat Transfer", *AIAA J.*, Vol. 18 (1982), p.1205.
10. Dwyer, H.A., "Grid Adaptation for Problems in Fluid Dynamics", *AIAA J.*, Vol. 22 (1984), p. 1705.

11. Rai, M.M. and Anderson, D.A., "Application of Adaptive Grids to Fluid Flow Problems with Asymptotic Solution", AIAA J., 20 (1982), pp. 496-502.
12. Gnoffo, P.A., "A Finite Volume, Adaptive Grid Algorithm Applied to Planetary Entry Flow Fields", AIAA J., Vol. 21 (1983), pp. 1249-1254.
13. Nakahashi, K. and Deiwert, G.S., "Three Dimensional Adaptive Grid Method", AIAA J., Vol. 24 (1986), pp. 948-954.
14. Nakahashi, K. and Deiwert, G.S., "Self Adaptive Grid Method with Application to Airfoil Flow", AIAA J., 25 (1987), pp. 513-520.
15. Abolhassiani, J.S., Smith, R.E. and Tiwari, S.N., "Grid Adaption for Hypersonic Flow", AIAA Paper No. No. 87-1169.
16. Jain, A.C., "Hypersonic Flow at Low Reynolds Number Near the Stagnation Point of a Blunt Body", Proceedings of the Summer Seminar on Fluid Dynamics, edited by P.L. Bhatnagar, Nallaris Printers, Bangalore (1968), pp. 65-80.
17. Jain, A.C., "Lectures on Reentry Aerodynamics", Vikram Sarabhai Space Centre, Trivandrum, 1980.
18. Jain, A.C., "A Comparative Study of Steady State and Time-Asymptotic Navier-Stokes Solution of Hypersonic Stagnation Merged Layers", Proc. of the 13th Int. Sym. on Space Tech. and Sci., Tokyo (1982), pp. 503-508.
19. Jain, A.C., "Hypersonic Merged Layer Flow over a Sphere", AIAA Paper 85-1031, 1985.
20. Jain, A.C. and Adimurthy, V., "Hypersonic Merged Stagnation Shock Layers", AIAA 6th Fluid and Plasma Dynamics Conference, Palm Spring, CA, July 16-18 (1973), AIAA Paper 73-639.
21. Jain, A.C. and Adimurthy, V., "Hypersonic Merged Stagnation Shock Layers, Part 1 : Adiabatic Wall Case", AIAA J., Vol. 12 (1974), pp. 342-347.
22. Jain, A.C. and Adimurthy, V., "Hypersonic Merged Stagnation Shock Layers, Part 2 : Cold Wall Case", AIAA J., Vol. 12 (1974), pp. 348-354.
23. Kumar, A. and Jain, A.C., "Non-equilibrium Merged Stagnation Shock Layers at Hypersonic Speeds", Int. J. Heat and Mass Transfer, Vol. 18, (1975), pp. 1113-1118.

24. Kumar, A. and Jain, A.C., "Hypersonic Radiating Merged Stagnation Shock Layer Near the Blunt Body Stagnation Region", *Int. J. of Heat and Mass Transfer*, Vol. 17 (1974), pp. 197-204.
25. Jain, A.C. and Kumar, A., "Hypersonic Radiating Merged Stagnation Shock Layer", *Second National Heat and Mass Transfer Conference*, I.I.T., Kanpur, Dec. 13-15 (1973).
26. Jain, A.C. and Prabha, S., "Hypersonic Second Order Merged Layer on Blunt Bodies", Submitted to the Department of Space, Government of India, Aug. 1982.
27. Jain, A.C. and Prabha, S., "A Comparative Study of Stagnation Point Hypersonic Viscous Shock Layer and Hypersonic Merged Layer Flows", *14th Int. Symp. on Rarefied Gas Dynamics*, Edited by H. Oguchi, Vol. (1984), pp. 241-248.
28. Jain, A.C. and Woods, H.G., "Investigation of Hypersonic Rarefied Flow on a Spherical Nose of AOTV", *NASA-SBIR, Phase 1*, Final Report submitted to NASA under contract NASA-37305, July, 1987.
29. Singh, J.S. and Jain, A.C., "Stagnation Point Merged Layer Flow With and Without Ablation", M.Tech. Thesis Report submitted to the Department of Aero Engg., 1987.
30. Levinsky, F.S. and Yoshihara, H., "Rarefied Hypersonic Flow Over a Sphere", *Hypersonic Flow Research*, edited by F.R. Riddel, Academic Press, New York, 1962, pp. 81-106.
31. Kennard, E.H., "Kinetic Theory of Gases", McGraw Hill Company Inc., 1962.
32. Liberstein, H.M., "A Course in Numerical Analysis", Harper and Row Publishers, Inc., New York, 1968, pp. 113.
33. Young, D., "Iterative Methods for Solving Partial Differential Equations of Elliptic Type", *Trans. American Math. Soc.*, Vol. 76 (1954), pp. 92-111.
34. Lew, H., "Method of Accelerated Successive Replacement Applied to Boundary Layer Equations", *AIAA J.*, Vol. 6 (1968), 929-931.
35. Dellinger, T.C., "Computation of Nonequilibrium Merged Stagnation Shock Layers by Successive Accelerated Replacement", *AIAA J.*, Vol. 9 (1971), 262-269.

3 99702

Thesis

620.0042 Date Slip 99702

M 931a This book is to be returned on the date last stamped.

AE-1900-m-MUR-APP